How fast can minibasins translate down a slope? Observations from 2D numerical models

Naiara Fernandez[1]*, Oliver B. Duffy[1], Christopher A-L. Jackson[2], Boris J.P. Kaus[3], Tim Dooley[1], Michael Hudec[1]

[1]Bureau of Economic Geology, Jackson School of Geosciences, The University of Texas at Austin, University Station, Box X, Austin, Texas, 78713-8924, USA

[2]Basins Research Group (BRG), Department of Earth Science & Engineering, Imperial College, Prince Consort Road, London, United Kingdom, SW7 2BP, UK

[3]Institute of Geosciences, Johannes Gutenberg University Mainz J.-J.-Becher-Weg 21, D-55128 Mainz, Germany

**Corresponding author: naiara.fernandez@beg.utexas.edu*

Running Title: Minibasin Translation

Keywords: salt tectonics; salt-detached slopes; continental slopes; salt velocity; minibasin translation;

Abstract

Minibasins are important features in salt-bearing basins and they are mostly found in salt-detached continental slopes where the sedimentary cover undergoes seaward translation. One question which is relevant to understand the structural evolution of salt-detached slopes is how fast can the sedimentary cover and the minibasins translate. The aim of this study is three-fold: 1) to compare minibasin downslope translation velocity with salt translation velocity; 2) to understand what controls minibasin translation velocity and 3) to understand how minibasins translating at different velocities can kinematically interact and modify strain patterns around them. To address these questions, we present a 2D numerical modeling study consisting of three simulation series. In the first series, we model a simple scenario where, as a result of gravity, a constant-thickness salt layer moves downslope on an inclined plane. In the second series, we use the same model geometry as in the first (i.e. constant thickness salt layer over an inclined plane), but we add a single, isolated minibasin at the updip portion of the slope. Different minibasin thicknesses, widths and densities are then tested, replicating how in natural salt basins, minibasin size (thickness and width) and fill (density as a proxy of lithology) vary as a function of their maturity, their structural position, and/or the overall regional geological setting in which they form and evolve. Finally, in the third series, we add three minibasins in the updip portion of the slope, and we assess how they interact as they translate downslope. In addition to parameters that control salt velocity on a slope, minibasin thickness is the main factor controlling minibasin velocity in the numerical models. Thicker minibasins translate slower than thinner minibasins. Findings from our numerical modelling approach have direct and significant implications for understanding minibasins behavior, kinematics and strain patterns on natural salt-detached slopes.

1. Introduction

Minibasins are important features of many salt-bearing basins and can form in different settings (i.e. marine and continental). Most minibasins, however, are found in salt-detached continental slopes, where linked kinematic systems can form (e.g. Jackson and Hudec, 2017). One characteristic of salt-bearing slopes is the seaward translation of the supra-salt sedimentary cover. A question inherent to salt-detached linked systems is how fast can the supra-salt sedimentary cover translate at present-day or over geological time. In order to understand how fast supra-salt sedimentary cover, including minibasins, can translate on salt-bearing slopes, we first must understand why and how fast salt can actually flow in such settings.

Over geological time scales, salt behaves as a fluid of very high viscosity. As a result, on salt-bearing continental slopes, salt moves down the slope due to gravity. On slopes, two main mechanisms drive salt flow: gravity spreading (deformation and collapse of a rock mass by its own weight) and gravity gliding (downslope translation of the rock mass over an inclined detachment) (e.g. De Jong and Scholten, 1973; Ramberg 1981; Brun and Merle, 1985). Distinguishing between these mechansims on natural examples of continental slopes is difficult, given it is likely that both processes contribute to the downslope flow of salt and the overlying sedimentary cover (e.g. Schulz-Ela, 2001; Rowan, 2004; Brun and Fort, 2011, 2012; Peel, 2014). In any case, as salt flows down the slope, the capping sedimentary cover on top also gets translated. One of the main outcomes of this style of salt-related deformation is the partitioning of continental slopes into three different domains: an up-dip extensional domain and a down-dip contractional domain, separated by a translational domain (Figure 1a).

So, gravity causes salt to flow down a slope, but how fast does it move? Direct observation of salt flow is restricted to areas where salt is exposed at the Earth's surface, such as in Iran, where aerial extrusions from salt diapirs form salt glaciers (e.g. Lees, 1927; Kent, 1958; Wenkert, 1979). These well-exposed salt structures enable direct measurements of salt flow at observational time scales (days to years) by means of different methods (i.e. satellite-based observations, alidade surveys), yielding values of 10-400 cm/yr (Wenkert, 1979; Talbot and Rogers, 1980; Talbot and Javis, 1984; Talbot et al., 2000). However, subaerial salt flow responds to complex dissolution-precipitation processes that change the rheology of the salt, and that makes extrapolation of short-term salt flow rates not applicable to salt flow over geological time scales (10^3-10^6 years) (e.g. Urai et al., 1984). In addition, the salt extrusion on the Zagros are driven by tectonic shortening which impacts the extrusion rate. Thus, our understanding of the rate of salt flow in the geological record is poor. When salt is buried under sediments, as it is the case in salt-detached slopes, salt flow has to be estimated by indirect observations. For example, in the northern Gulf of Mexico salt canopy, estimates of salt advance velocities over geological times rely on well-data-contrained age and seismic based observations of the cutoffs of the stratigraphic sequence over which the salt was advancing as it moved downslope (e.g. Tauvers, 1993). Advance rates of salt sheets using structural restorations of geological sections constructed from seismic interpretations provide long-term strain rates that range between 0.1-2 cm/year (e.g. Diegel et al., 1995, Peel et al., 1995; Schuster et al., 1995; Jackson and Hudec, 2017 and references therein). These values are 2-3 orders of magnitude slower than the ones measured for subaerial salt glaciers.

Constraining how fast salt moves at geological time-scales (thousands to millions of years) is thus challenging and has many uncertainties. Constraining the translation velocity of the sedimentary cover that overlies salt in the translational domain of a continental slope is even more challenging and uncertain. Compared to the updip extensional and the downdip compressional domains, clear indicators of displacement magnitudes (e.g. fault cutoffs) are usually absent in the translational domain (e.g. Jackson and Hudec, 2005). This is even more true if instead of a continuous cover, the domain is populated with minibasins that are only partially interconnected, as is the case of minibasin provinces located in continental slopes (e.g. Northern Gulf of Mexico; Figure 1b). It is not unusual for velocity estimates of the sedimentary cover in the translational domains, to be inferred from observations of salt-detached ramp syncline basins and rafted minibasins (e.g. Jackson and Hudec, 2005; Evans and Jackson, 2019; Pichel et al., 2019; Jackson et al., 2010; Fiduk et al., 2014; Pilcher et al., 2014). Translation rate estimates of sedimentary cover based on reconstructed cross-sections provide velocities in the ranges of 0.1-1 cm/year (e.g. rafted minibasin in the Gulf of Mexico; Jackson et al., 2010). However, minibasin translation velocities may not remain constant through time, and it is presumed that minibasin translation rates will dramatically decrease as they are close to welding at their base (e.g. Wagner and Jackson 2011). Furthermore, the downslope transation of minibasins can be obstructed by base-salt relief or friction associated with primary welding, processes that result in locally complex strain patterns on the slope (e.g. Duffy et al., 2020) (Figure 1c).

One question that has not been explicitly addressed before is, how different the velocity of downslope-flowing salt is from the velocities of overlying minibasins. More specifically, do minibasins move faster or slower than the surrounding salt? How do minibasin thickness, geometry and density affect how fast they translate before they are close to welding? Understanding why and how salt and minibasins move at different velocities is relevant for understanding the evolution of salt-detached slopes.

Ultimately, the absolute distance a minibasin can travel on a slope is constrained by its maximum translation velocity, as well as the time over which translate. Thus, having a better understanding of what controls minibasin translation velocity will help contrain structural restorations of salt basins. Furthermore, if minibasins translating at different velocities can coexist on a slope, this can result in differential translation between minibasins and complex strain patterns around them (e.g. Krueger, 2010; Duffy et al., 2020).

The aim of this study is three-fold: 1) to compare minibasin downslope translation velocity with salt translation velocity; 2) to understand what controls minibasin translation velocity and 3) to understand how minibasins translating at different velocities can kinematically interact and modify strain patterns on the slope.

We present a 2D numerical modeling study consisting of three simulation series. In the first series, we model a simple scenario where, as a result of gravity, a constant-thickness salt layer moves downslope on an inclined plane (Figure 2a). This scenario reflects a simplification of the translational domain of a salt-detached continental slope. For this particular scenario, an analytical solution exists (e.g. Turcotte and Schubert, 2001), which we use to benchmark our numerical models. In the second series, we use the same model geometry as in the first (i.e. constant thickness salt layer over an inclined plane), but we add a single, isolated minibasin at the updip portion of the slope. Different minibasin thicknesses, widths and densities are then tested, replicating how in natural salt basins, minibasin size (thickness and width) and fill (density as a proxy of lithology) vary as a function of their maturity, their structural position, and/or the overall regional geological setting in which they form and evolve. Finally, in the third series, we add three minibasins in the updip portion of the slope, and we assess how they interact as they translate downslope.

2. How fast does salt flow down a slope?

We are first interested in understanding regional-scale salt flow on salt-detached slopes. We can consider the salt-detached slope as equivalent to an inclined plane overlain by a viscous fluid layer of constant thickness (e.g. Turcotte and Schubert, 2001). The inclined plane would be analogous to the slope, and the viscous layer would be analogous to the salt (Figure 1 and 2a). A schematic cartoon of the setup is shown in Figure 2a, where, $\mathbf{u}$ is velocity, $\boldsymbol{\rho}$ is salt density, $\boldsymbol{\mu}$ is salt viscosity, $\mathbf{g}$ is gravity, $\boldsymbol{\alpha}$ is the slope angle and $\mathbf{h}$ is the salt layer thickness.

Using a fluid dynamics approach, the velocity profile of the unidirectional flow of a viscous fluid down an inclined plane can be obtained assuming the following conditions: the flow occurs in a layer of constant thickness (h) viscous fluid; no-slip condition (u = 0) at y=h; and free-surface (τ = 0) condition at y=0.

$$u = \frac{\rho g \sin\alpha}{2\mu}(h^2 - y^2) \qquad (1)$$

The equation can be solved for the maximum and mean velocity in the layer, and we obtain:

$$u_{max} = \frac{\rho g \sin\alpha}{2\mu}(h^2) \quad (2)$$

$$u_{mean} = \bar{u} = \frac{\rho g h^2 \sin\alpha}{3\mu} \qquad (3)$$

Derivations of the equations Eq. (1), Eq. (2) and Eq. (3) are described in Appendix A. These equations can be used to calculate both the maximum and mean velocity of the salt on a salt-detached slope, if we use the appropriate values for the parameters (within the ranges observed in the natural examples described above). A normalized analytical velocity profile can be obtained from Eq. (1) by plotting it in the non-dimensional y/h and u/u_{max} axes (Figure 2b). The maximum velocity occurs at the surface of the salt, where y = 0 and the velocity is zero at y=h (Figure 2b). The average value of the salt velocity profile corresponds to $u_{mean} = \frac{2}{3} u_{max}$. Eq. (1) is also used to perform calculations for a combination of the main parameters: salt thickness and slope angle. We use a range of salt thicknesses (0.1-5 km) and slope angles (0.1-6°) that comparable to those encountered on natural salt-detached continental slopes (e.g. Peel, 2014 and references therein). Salt density is taken to be 2200 kg m^{-3}, an appropriate value for a halite salt-rock with 5 % of impurities (e.g. Gevantman, 1981; Jackson and Hudec, 2017). The rheology of salt at geological time scales is still widely debated and depends on many factors, including the tectonic setting (e.g. Urai et al., 2008.; Jackson and Hudec, 2017). For this particular study, we model the salt as a linear-viscous material characterised by a viscosity of 10^{18} Pa s (e.g. Mukherjee et al., 2010 and references therein). This is an over-simplification, but it facilitates comparison with the existing simple analytical solution. The mean and maximum velocity salt velocities calculated for the given parameters are plotted in Figure 3 (maximum velocity contours represented by solid lines, mean velocity contours by dashed lines). For example, for a salt layer of 4 km thickness, with a slope angle of $\alpha = 2°$ (grey circle, Figure 3), the analytical solution predicts a maximum salt velocity of 18.99 cm/year at the top of the salt layer, and a mean salt velocity of 12.66 cm/year. For same angle of slope but salt layer of 2 km, the maximum salt velocity is 4.75 cm/year and mean salt velocity is 3.17 cm/year.

The analytical solution serves as a benchmark for our numerical experiments (see below). We use the 2D finite-element code MVEP2 (Thielmann & Kaus 2012; Johnson et al. 2013). MVEP2 solves the equations of conservation of mass and momentum for incompressible materials with visco-elasto-plastic rheologies, and employs Matlab-based solvers MILAMIN (Dabrowski et al. 2008) for efficiency. The code uses a Lagrangian approach, where material properties are tracked by randomly distributed markers that are advected according to the velocity field that is calculated in a deformable numerical grid. Remeshing of the grid is performed every time step. The method and numerical implementation are explained in detail in Kaus (2010).

The numerical model domain is a 120 km-wide, 15 km-high modeling box (Figure 4a). All the boundary conditions of the modeling box are set to free-slip (velocity is parallel to the boundary). The geometry within the model box consists of an inclined basement capped by an undeformed, constant-thickness salt layer (Figure 4a). In numerical simulations with this initial geometry, salt will immediately flow downslope due to gravity, causing salt to thicken at the base of the slope, and thin at the upper slope (Figure 4b). To keep the thickness of salt constant, an internal boundary condition has been applied to the interface between salt and air/water (Figure 4c and d). The aim of the internal boundary condition is to "remove" salt flowing above the initial inclined topography at the base of the slope, and "add" salt to fill in the area at the top of the slope depleted of salt below the initial topographic level (Figure 4d). This boundary condition ultimately produces a continuous flow of salt on the slope, keeping the salt thickness constant such that it is comparable to the scenario for which the analytical solution exists (compare Figure 2a and Figure 4c). The variables tested in these numerical simulations are the following: inclination of the slope (α), salt viscosity (μ) and density (ρ) and thickness of salt layer (h). The results of numerical experiments are compared with the predictions of the analytical solution to test the appropriateness of the numerical simulations (Figure 2b). Velocity profiles obtained from numerical simulations where salt thickness is maintained constant plot on top of, or very close to, the velocity profile obtained analytically (Figure 2b). With a resolution of 1000 X 150 nodes (element size of 120 m x 100 m), the deviance of the numerical solution from the analytical solution is <1 %.

The central portion of the slope in the numerical simulations (between -40 km to 40 km) has a salt velocity profile that remains constant through time, not influenced by edge or boundary effects resulting from the salt deflation and inflation processes, or the applied internal boundary condition (Figure 4c). We thus consider this portion of the numerical domain to be an appropriate representation of the translational domain of a continental slope (Figure 1a). In such a domain, the effects of the updip extensional and downdip compressional domains are far enough away as not to affect the dynamics of salt flow and translation in our numerical models (Figure 4c). Herein, we will focus the description of the numerical simulations on this central portion of the slope.

3. How fast do Minibasins Translate Downslope?

The series of numerical simulations described in this section aim to understand what controls the downslope translation velocities of minibasins on a salt-detached slope. The geometry of the numerical models is same as the one used to reproduce the analytical solution of salt flowing on an inclined plane (Figure 3a). However, in this series, a single isolated minibasin is added to the upper slope in each of the simulations. Although minibasins are rarely isolated in nature, these simulations aim to develop an understanding of the fundamental controls on minibasin downslope translation, in the absence of neighbouring minibasins. Furthermore, it is important to note that the minibasins used in the simulations approximate rounded-at-the-base semi-circles. Two model sub-series are discussed: 1) in which the density of the minibasins is equal to that of the salt (i.e. neutral-buoyancy minibasins). The aim of this sub-series is to understand the effect of minibasin geometry (mainly thickness and width) on their translation velocity, and; 2) in which the minibasin density differs from the salt, such that the minibasin either subsides (i.e. minibasins are denser than salt) or rises (i.e. minibasins are less dense than salt) as it translates downslope.

All simulations described here have a slope of α = 2°, salt viscosity of $\mu_{salt} = 10^{18}$ Pa s, salt density of ρ_{salt} = 2200 kg/m^3 and a salt thickness of H_{salt}= 4 km. The minibasins in the numerical simulations are modelled as being visco-plastic with viscosity of $\mu_{minibasin} = 10^{25}$ Pa *s* and friction angle ϕ = 30° and cohesion C = 20 MPa, following the Drucker-Prager yield criterion. Simulations are run for several hundred time-steps. The last time-steps are discarded and are not described here, because as the minibasins approach the base of the slope they get closer to the area where the effects of the internal boundary conditions would be noticed. For each of the simulations the velocity field calculated in the code is used to extract the translation velocity of the minibasin at each time-step. Next, we describe the observations from each model sub-series.

3.1 Models with Neutral-Buoyancy Minibasins

In models of neutral buoyancy minibasins, $\rho_{minibasin} = \rho_{salt}$ = 2200 kg/m^3, minibasins translate downslope as the salt flows. Because the density of the minibasins is equal to that of the salt, they do not subside or rise above salt (Figure 5). After around 200,000-400,000 years, the minibasins have traversed the central portion of the slope (Figure 5). Two different minibasin thicknesses are discussed next. The initial thickness of the minibasins is either 2300 m (herein referred to as 'thin') or 3300 m (herein referred to as 'thick') (if other thickness value is used, it will be specified in the text). Images of the simulations are shown for the initial geometry and for two time-steps, after 200,000 and 400,000 years, along with their corresponding velocity plots (Figure 5a, b). Our results show how the thin minibasin has translated further downslope than the thick minibasin during the same time interval (compare Figure 5a and b). The translation velocity of neutral buoyancy minibasins remains nearly constant throughout the simulation (Figure 5c, d). The mean velocity of the minibasins during this translational stage is 8.26 cm/year and 14.58 cm/year, for the thick and thin minibasins respectively (Figure 5c, d). In this particular example, it means that the thin minibasin, despite being 30 % thinner than the thick minibasin, translates 75% faster. When compared to the velocity obtained for salt (i.e. 18.99 cm/year maximum velocity; 12.66 cm/year mean velocity), we note that both the thick and thick minibasins translate at a velocity lower than the theoretical maximum salt velocity (Eq. (2)). However, while the thick minibasin translates at a velocity lower than the theoretical mean salt velocity (Eq. (3)), the thin minibasin translates faster than the theoretical mean salt velocity.

These minibasin velocities are calculated from simulations where salt topography is kept constant (Figure 5). The effect of a truly free surface that allows for the build-up of salt topography in the models has been tested and the results for the thick minibasin are shown (Figure 6a). As the average velocity of the thick minibasin is dramatically slower than velocity of the shallow (i.e. upper) portion of the salt, the faster-flowing salt up-dip of the minibasin extrudes onto the minibasin (Figure 6a). The effect of the free-salt topography is a slight increase of the minibasin velocity through time (Figure 6b). However, for simplicity, we will mainly focus on the results from the simulation in which salt thickness is kept constant (unless otherwise stated).

3.2 Models with Subsiding and Buoyant Minibasins

In models where minibasins have a density different to that of the salt, they will either subside into salt (if denser than salt) or rise buoyantly (if less dense than salt) as they translate downslope. A snapshot after the same time interval in simulations with subsiding and buoyant thick and thin minibasins is shown in Figure 7. The minibasins in the Figure have density values of $\rho_{minibasin}$ = 2000, 2100, 2200 2300, 2400 and 2500 kg/m^3 (salt density being ρ_{salt} = 2200 kg/ m^3). Our models show that, unsurprisingly, the denser the minibasin, the faster it subsides into salt. In our simulations, sediment fills the accommodation created as a minibasin subsides. Accommodation in downslope-translating minibasins is invariably created on the up-dip side of the minibasin. By the end of the simulation, the minibasins are overlain by a wedge-shaped sediment package that thickens up-dip (light brown color wedge shapes seen in Figure 7). The denser the minibasin is initially, the thicker the final wedge-shaped package is at the end of the simulation (Figure 7). When the results of simulations with minibasins of different densities are compared at the same time step, it can be observed that the amount of distance travelled by the minibasins differs (Figure 7). The denser the minibasin the shorter distance the minibasin it translates (Figure 7). For example, increments of 100 kg/m^3 in initial minibasin density (4.5 % increase) result in the minibasins translating 15-17% less. As expected from the experiment with neutral-density minibasins of the previous section, the thinner minibasins, which in this case are the less dense ones, translated further.

We can further assess the effect of density on minibasin translation velocity by looking at temporal changes in velocity (Figure 8). This shows that subsiding minibasins tend to decrease their translation velocity as they subside and become thicker (Figure 8). Conversely, buoyant minibasins tend to increase their velocity through time as they rise over salt (Figure 8). However, the temporal *increase* of translation velocity in buoyant minibasins is small compared to the velocity *decrease* through time associated with subsiding minibasins (Figure 8).

4 What controls minibasin velocity?

Because the minibasins in the simulations are embedded in the flowing salt, the first-order control on minibasin velocity in the absence of any other external factor (i.e. tectonics) is presumably the velocity of the flowing salt. A theoretical salt velocity profile, and its corresponding maximum and mean salt velocities can be calculated from the analytical solution (Eq. (1); Figure 2 and Eq. (2) and (3); and Appendix A). However, that analytical solution is a 1D channel flow approximation, where there is no shear stress variation in the direction parallel to the slope (see Appendix A for details). Given this constraint, we now discuss how the thickness (normalized over salt thickness) and aspect ratio of minibasins affect their translation velocity, and how their velocity relates to the analytically predicted salt velocity.

The sketch in Figure 9 illustrates a constant thickness salt layer on a slope with a minibasin embedded in the salt. The thickness of the minibasins at its center is T_{mb}, thus, the basal position of the minibasin in a y profile would correspond to y = T_{mb}. This position (y= T_{mb}) can be used to conceptually divide the salt layer profile into two different portions: an upper salt portion, from 0 to y= T_{mb} and a lower salt portion from y= T_{mb} to y=h. Various theoretical salt velocity profiles (and corresponding maximum and mean values) can be calculated considering the salt layer to be split into two portions at y= T_{mb}. The theoretical profiles are illustrated in Figure 9.

The analytical salt profile described by Eq. (1) can be used to calculate the theoretical salt velocity profile for the complete salt layer (thickness h). Then, the mean salt velocity of the upper portion of this entire salt velocity profile can be calculated and we will refer to this mean velocity as, $\bar{u}_{mb}$. Similarly, Eq. (1), can be used to obtain the mean velocity of a theoretical salt velocity profile of the upper salt portion (h'=y=T_{mb}). We refer to this mean velocity as $\bar{u}_{h'=y}$. The corresponding mathematical expressions of these definitions are described in detail in Appendix A.

Next, we compare the results from the numerical simulations of minibasin translation, with these analytically-predicted mean velocity profiles.

4.1 Minibasin Thickness

Numerical simulations with neutral buoyancy minibasins of different thicknesses have been used to extract the minibasin velocity after the initial time-step, for three different initial model geometries (H=4 km and $\alpha = 4°$; H=4 and $\alpha = 2°$; H=2 and $\alpha = 4°$). Because, we have shown that the velocity of neutral buoyancy minibasins in the numerical models is approximately constant through time (see Figure 5), we have taken the value of one-time step in each simulation. Each numerical model result is plotted in Figure 10a. Numerically calculated velocities fall on top of one of the analytically calculated lines (Figure 10a). Thus, the velocity of neutral buoyancy minibasins for minibasin whose thickness is less than 70% of the total salt thickness is described by the following equation (check Appendix A for details):

$$u_{mb} = u_{\max h} - \bar{u}_{y=Tmb} = \frac{\rho\, g\, sin\alpha\, h^2}{\mu\, 2} - \frac{\rho\, g\, sin\alpha\, y^2}{\mu\, 3} \quad (4)$$

It must be noted that minibasin velocity calculated from the numerical models deviates from the line described by Eq. (4) when the minibasin thickness approximates the salt thickness (minibasin thickness T_{mb}>70% H) (Figure 10a). This implies that in the numerical models there is an effect of the base salt boundary, an important feature not captured by the analytical solution. The effect of the proximity of the minibasin to the base-of-salt is to slow down the translation velocity (e.g. Wagner & Jackson, 2011).

Compared to neutral-density minibasins, we have seen that, subsiding minibasins increase their thickness and decrease their translation velocity through time. We have plotted the evolution of thickness and corresponding minibasins velocity in numerical simulations with subsiding minibasins, for minibasins with a density = 2500 kg/m^3 (Figure 10b). The results of three numerical simulations with different initial minibasin thicknesses of 1300 m, 2300 m and 3300 m are shown in Figure 10b. Subsiding minibasins follow the analytical curve described by Eq. (6) as they increase their thickness. However, as for the neutral minibasins, the effect of the model base (base-of-salt) is to dramatically decrease minibasin translation velocity (Figure 10b). This more pronounced decrease in minibasin translation velocity occurs when subsiding minibasins reach a thickness that is close to that of the salt layer (>70%), at which point the model results deviate from the analytical solution of Eq. (6) (Figure 10b).

The graphs of Figure 10, can be used in conjunction with Eq. (1), to predict the minibasin velocities that would be expected in the numerical models, without actually performing new simulations. For a given minibasin thickness (normalized over salt thickness), from the graphs of Figure 10, we can obtain the minibasin velocity (normalized over maximum analytical salt velocity). That normalized minibasin velocity can be converted to an actual velocity (e.g. cm/year) by using for the conversion the analytical maximum salt velocity as calculated from Eq. (1).

4.2 Minibasin Aspect Ratio

As mentioned previously, the minibasins used in the simulations in Figs 5, 6 and 7 are approximated as rounded-at-the-base semi-circles. This shape minimizes the effect of the basal viscous drag, as the contact surface in the direction of the salt flow, which is parallel to the slope, is almost infinitely small. Increasing the aspect ratio of the minibasins and making them wider increases the contact length between the minibasin and the base salt, thus should increase viscous drag and potentially slow down minibasin translation velocity (Figure 11a). We test this effect using numerical simulations of minibasins of different aspect ratios and basal lengths and note small differences in their translation velocities (Figure 11a). Although, the overall effect of increasing minibasin aspect ratio is much less dramatic when compared to the effect of increasing minibasin thickness, it is of note. If a minibasin is thin and the effect of the base-of-salt is negligible (i.e. the kinematics can still be described by the dashed red curve given by Eq. (4), Figure 10a), the aspect ratio has almost no influence on translation velocity. For the example of the thin minibasin with a thickness T_{mb} = 1300 m, the minibasin thickness over salt relation is T_{mb}/H_{salt} ~=0.325, and there is no influence of the base-of-salt (Figure 10a, dashed red line). In such a case, increasing the minibasin width to double the original width (factor of 2 increase), results in a <5 % decrease in translation velocity (Figure 11b; line described by grey circles for T_{mb}/H_{salt} ~=0.325). If instead, the initial minibasin is thick and its velocity is already affected by the base-of-salt as described in previous section (i.e. deviates from Eq. (4), Figure 10a), then changes in aspect ratio become more significant. For example, for a minibasin with T_{mb} = 2300 m and T_{mb}/H_{salt} ~=0.825, increasing minibasin width by a factor of 2.5 results in a 25 % decrease in translation velocity (Figure 11b; line described by black stars for T_{mb}/H_{salt} ~=0.825). This effect can be explained by the fact that we are increasing the surface of the minibasin exposed to viscous drag.

5 Strain patterns around minibasins moving at different velocities

We have demonstrated that neutral-density minibasins of different initial thicknesses translate at different velocities. We have also shown that subsiding minibasins decrease their velocity as they increase their thickness, as well as providing new intra-slope accommodation as they translate downslope. Now we explore how minibasins interact as they translate downslope at at different velocities. Can the different translation velocities result in minibasins converging or diverging from each other as they travel downslope? If so, how does this influence local strain patterns?

We can hypothesise that if a minibasin translates faster than another minibasin further upslope of it, then over time, the distance between the two will increase. In contrast, if the upslope minibasin is faster than the downslope minibasin, it follows that the opposite will occur and the minibasins will converge and possibly collide. To test these hypotheses and illustrate the resulting strain patterns around minibasins moving at different velocities, we performed a final series of numerical models comprising a chain of three neutral-density minibasins of different thicknesses (Figure 12a, b). A thin minibasin located upslope (MB1) is followed downslope by a thick minibasin (MB2), and a third thin minibasin located even further downslope (MB2) (Figure 12a, b). The minibasins are separated by diapirs labelled as D1 and D2 in Figure 12a, b. Given this minibasin configuration, we test two scenarios: one in which the diapirs between minibasins contain no roof, and other in which the diapirs between the minibasins are overlain by a roof of 500 m of the same materials that form the minibasins (Figure 12a, b).

We first discuss the case with no roof over the diapirs. At the beginning of the simulation, the minibasins translate downslope (Figure 12a). The evolution of the velocity for each of the minibasins is shown in Figure 12c. MB1 and MB3, the thin minibasins, translate faster than MB2, the thick minibasin.

Because the thinner minibasins are faster than the thicker one, the furthest downslope minibasin (MB3) diverges from the thick minibasin located just upslope (MB2). Conversely, the upslope minibasin MB1 converges with the thick minibasin (Figure 12a). The diapir between the converging minibasins is squeezed. This convergence and divergence between the minibasins can be analyzed in terms of strain and strain rate, as calculated by the change in distance between the minibasins and is shown in Figure 13. Convergence between the minibasins can occur because of the shortening accommodated by squeezing the intervening diapir, while the divergence must be accommodated by extension and widening of the intervening diapir. When no roof on top of the diapirs is present, the shortening and extension associated with converging and diverging minibasins is cryptically accommodated by the intervening salt. It would be very difficult to detect this deformation in natural systems.

In the second case, in which the diapirs are covered by a roof and the minibasins are thus physically connected, this roof records the resulting strain patterns (Figure 12b). Interestingly, at the very beginning of the simulations, when the roof between the minibasins is still undeformed, the minibasins essentially behave as a single mechanical unit, with equal initial velocities. This is specially true between converging MB1 and MB2 (Figure 12d). As the minibasins start translating downslope, the thin minibasins move faster than the intervening thick minibasin. As in the example with no roof, the upslope thin minibasin (MB1) starts to converge with the slower-moving thick minibasin (MB2). In contrast, the downslope thin minibasin (MB3) diverges from the slower-moving upslope minibasin (MB2). The different translation velocities between the minibasins are again accommodated by deformation of the intervening diapirs. However, in this case, the presence of the roof on top of the diapirs results in the development of an additional suite of structures. For example, the roof of diapir D2 stretches and breaks as the thin, faster minibasin MB3 diverges from MB2 (Figure 12b). In contrast, the roof of diapir D1 folds to accommodate the shortening resulting from the upslope, relatively fast, thin minibasin (MB1) converging with the thicker, slower-moving minibasin downslope (MB2) (Figure 12b). The resulting strain and strain rate evolution of the diapirs with roofs is different to the case where the diapirs lack roofs (Figure 13). Much more strain, at higher strain rates, can be accommodated due to the different translation velocities when the diapirs do not have roof, and when all the deformation can be cryptically accommodated by squeezing or stretching the salt (Figure 13). If diapir roofs were sufficiently thick to be mechanically too strong to accommodate any deformation due to converging or diverging minibasins, the chain of minibasins would translate as a single mechanical unit.

6 Implications for minibasin kinematics on slopes

As salt flows down a slope, minibasins that have developed in the salt layer are also translated. We modelled simple scenarios where the base-of-salt in the slope is smooth. A striking finding from our modelling is that even with a smooth base-of-salt, minibasin translation can still be complex as minibasins of different thicknesses and geometries can translate at different velocities. Furthermore, minibasin translation can decrease dramatically as the salt beneath is thinned, eventually freezing in place when the minibasin welds (e.g. Krueger, 2010; Wagner and Jackson, 2011). The observations from the numerical models are synthesized into a schematic review figure (Figure 14a,b), where the effects of minibasin thickness, width and density on the final minibasin velocity are conceptualized. Minibasins translating at different velocities can converge or diverge, and hence modify strain patterns around then (Figure 12, 13). Shortening is accommodated in between two converging minibasins, while extension occurs in between two diverging minibasins (Figure 14c). This localized shortening and extensional strains can be cryptic if the salt lacks a roof, with minibasin spacing erroneously interpreted as being an original feature.

However, the base-of-salt in natural salt basins can be highly rugose and can have considerable relief. When minibasins translate downslope over a rugose base-of-salt, if thick enough, the minibasin can weld at its base, or buttress against a high-relief base-salt feature, obstructing the minibasin from further downslope translation (e.g. Krueger, 2010; Wagner and Jackson, 2011; Duffy et al., 2020). The complex deformation patterns that result from different degrees of minibasin obstruction at both the minibasin-scale and the sub-regional scale have been recently described in detail in an area where the base-of-salt has very high relief (i.e. the northern Gulf of Mexico canopy; Duffy et al., 2020, Fernandez et al., 2020). Minibasin obstruction results in shortening immediately upslope of the obstructed minibasin, and extension on the downslope side of the obstructed minibasin (e.g. Duffy et al., 2020) (Figure 1c). The interactions between minibasins and the base-of-salt and the potential for minibasins to be obstructed, is important when trying to understand strain patterns around minibasins.

Depending on the initial configuration of minibasins translating at different velocities over a smooth base-of-salt slope, strain patterns can be akin to those described near obstructed minibasins: up-dip shortening and down-dip extension (compare Figures 1c and 14c). Thus, when attemping understand strain patterns and minibasin kinematics on salt-detached slopes, it is important to consider the influence of one, or a combination of: i) minibasin obstruction and interaction with the base-of-salt (*sensu* Duffy et al, 2020); and ii) kinematic interactions between minibasins translating at different velocities in the absence of base-of-salt relief (this study).

The key finding of this work (that minibasins can translate downslope at different velocities) has been demonstrated in 2D with an analytical solution and numerical models. However, salt flow is three-dimensional. We speculate that in the case of isolated minibasins in 3D, the fundamental principles outlined in this study still apply, notably in terms of how the minibasin velocity relates to the overall theoretical salt velocity profile. The isolated minibasins will translate at a slower velocity than the maximum salt velocity (at the salt surface). In 3D, however, increasing minibasin thickness, length (along slope direction) or width (along strike direction), will increase the surface area exposed to viscous drag, more than it would proportionally in 2D.

The implications of considering the three-dimensional behaviour of minibasins extend beyond simple consideration of their velocity as it may also influence minibasin kinematics and strain patterns. For example, different translation velocities are also possible between neighboring minibasins that are not necessarily located directly upslope or downslope of one another (i.e. as in our numerical simulations). Where minibasins are slightly offset from the downslope pathway of neighboring minibasins, additional strike-slip components will be added to the shortening and extension zones. The complex three-dimensional strains due to differential translation of the sedimentary cover have been previously described using seismic reflection data imaging natural systems (e.g. Krueger, 2010; Duffy et al., 2020; Fernandez et al., 2020), and have also been described from physical models (Dooley et al., 2019; Duffy et al., submitted). In those previous works, strike-slip patterns around minibasins are discussed within the context of minibasins obstructed or stopped due to welding. However, the different translation velocities between minibasins may be an important contributor to such complex strains.

7 Summary

Due to the viscous behavior of salt over geologic time and the effect of gravity, a layer of salt lying over an inclined plane flows downslope. Assuming that the thickness of the salt layer is kept constant, the velocity of the flowing salt can be described by a mathematical expression. Such analytical expression predicts a velocity profile with a maximum salt velocity at the top of the salt layer (salt topography), decreasing to zero at the base of the salt layer. We have reproduced the predictions of the analytical solution for salt flow with a 2D numerical simulations of a salt layer overlying an inclined plane.

Returning to our initial question of how fast can minibasins translate on a slope, the answer is that it depends on a number of factors. At a first order approach, the comparison of our numerical simulations with the analytical solution show that minibasins travel at a slower velocity than the theoretical maximum salt velocity (Figure 10). On top of that, there are a number of factors to consider that will affect minibasin velocity (summarized in Figure 14a).

Minibasin thickness is the main factor controlling minibasin velocity. Thicker minibasins translate slower than thinner minibasins. Furthermore, when the base of the minibasins is close to the base of the salt, the velocity is further decreased. This is true for all minibasins regardless of their density or shape.

In the case of neutral-density minibasins, their thickness remains constant during their translation, and so does their translation velocity. If minibasins are of non-neutral-density, whether they be subsiding or rising, their salt-embedded thicknesses changes during their translation, and so does their velocity. Minibasins that are denser than salt subside into salt as they translate, and if new sediments are deposited, their thickness increases. As thickness of subsiding minibasins increases, their translation velocity decreases through time. Regardless of the density structure of a minibasin, their velocity can be predicted analytically, as long as they are far enough (minibasin thickness is less than 70% salt thickness) from the base of salt (Eq. (4), Figure 10a,b).

When the minibasin is thick enough so that it is close to the base of salt, minibasin velocity decreases more dramatically than as predicted by Eq. (4) (Figure 10a,b). For such cases, the shape or aspect ratio of the minibasin is another factor to be considered. The aspect ratio of minibasins controls the area or length of the minibasin contact surface at the direction parallel to salt flow exposed to viscous drag. Longer minibasins, have more contact surface. The longer the contact surface, the greater the effect of viscous drag at the base of the minibasin is, and therefore, the more the minibasin velocity is reduced (Figure 11).

The findings from our numerical modelling approach have direct and significant implications for understanding minibasins behavior, kinematics and strain patterns on natural salt-detached slopes. Minibasins of different maturity can coexist at any given time in the translational domain of a salt-detached continental slope (e.g. Ge et al., 2020). Such maturity affects their thickness and their density structure. Our study shows that such differences will result in minibasins translating downslope at different velocities. Depending on the initial configuration of the minibasins, this may result in convergence and divergence of minibasins, and minibasins will be able to translate past another in a three-dimensional configuration. These minibasin kinematics will result in deformation being accommodated by the intervening salt structures (e.g. diapirs), or by the overlying sedimentary cover (e.g. diapir roof). When interpreting strain patterns around minibasins, it is important to consider that shortening and extensional deformation can be the result of minibasins translating at different velocities in continental slopes.

Acknowledgements

MVEP2 numerical code is public and available from https://bitbucket.org/bkaus/mvep2/. The simulations shown in this study were performed with a version of MVEP2 that was checked from the repository on July 19th 2019, with commit ID number [48165b4]. Thanks to WesternGeco for providing permission to show the 2D seismic section. The project was funded by the Applied Geodynamics Laboratory (AGL) Industrial Associates program, comprising the following companies. For an updated list of sponsors check http://www.beg.utexas.edu/agl/sponsors. The authors received additional support from the Jackson School of Geosciences, The University of Texas at Austin.

Appendix A: Derivations of Equations

References

Brun, J.P. and Fort, X., 2011. Salt tectonics at passive margins: Geology versus models. Marine and Petroleum Geology, 28(6), pp.1123-1145. Doi: 10.1016/j.marpetgeo.2011.03.004

Brun, J.P. and Fort, X., 2012. Salt tectonics at passive margins: geology versus models–Reply. Marine and Petroleum Geology, 37(1), pp.195-208. Doi: 10.1016/j.marpetgeo.2012.04.008

Brun, J.-P., and Merle, O., 1985, Strain patterns in models of spreading-gliding nappes, Tectonics, 4 (7), 705-719, doi: 10.1029/TC004i007p00705.

Dabrowski, M., Krotkiewski, M. & Schmid, D.W. 2008. MILAMIN: MATLAB based finite element method solver for large problems. Geochemistry, Geophysics, Geosystems, 9, Q04030, Doi: 10.1029/2007GC001719

De Jong, K. A., and Scholten, R. 1973. Gravity and tectonics. New York, John Wiley and Sons, 502 p.

Diegel, F.A., Karlo, J.F., Schuster, D.C., Shoup, R.C. and Tauvers, P.R., 1995. Cenozoic structural evolution and tectono-stratigraphic framework of the northern Gulf Coast continental margin. In. M. P. A. Jackson, D. G. Roberts, & S. Snelson (Eds.), Salt Tectonics: A Global Perspective, AAPG Memoir, Vol. 65, (pp. 109–151). Tulsa, OK: American Association of Petroleum Geologists.

Dooley, T. P., O. B. Duffy, M. Hudec, and N. Fernandez, (2019), Shortening of Diapir Provinces: Translation, Tilting and Rotation of Minibasins in Isolated Minibasin System, *AAPG Annual Convention and Exhibition, San Antonio, Texas*, DOI:10.1306/11229Dooley2019

Duffy, O.B., Fernandez, N., Peel, F.J., Hudec, M.R., Dooley, T.P. and Jackson, C.A.L., 2020. Obstructed minibasins on a salt-detached slope: An example from above the Sigsbee canopy, northern Gulf of Mexico. *Basin Research*, *32*(3), pp.505-524. Doi: 10.1111.bre.12380

Duffy, O.B., Dooley, T.P., Hudec, M.R., Fernandez, N., Jackson, C.A.L., Soto, J.I. 20XX. Structural evolution of salt-influenced fold-and-thrust belts: principles in salt basins containing isolated minibasins. Preprint. Doi:10.13140/RG.2.2.10203.59682.

Fernandez, N., Duffy, O.B., Peel, F. and Hudec, M.R., 2020. Influence of minibasin obstruction on canopy dynamics in the northern Gulf of Mexico. *Basin Research*. Doi: 10.1111.bre.12480

Fiduk, J. C., Clippard, M., Power, S., Robertson, V., Rodriguez, L., Ajose, O., Smith, D. (2014). Origin, transportation, and deformation of mesozoic carbonate rafts in the Northern Gulf of Mexico. GCAGS Journal, 3, 20–32.

Ge, Z, Gawthorpe, RL, Zijerveld, L, Oluboyo, AP. Spatial and temporal variations in minibasin geometry and evolution in salt tectonic provinces: Lower Congo Basin, offshore Angola. *Basin Res*. 2020; 00: 1– 18. Doi:10.1111/bre.12486

Gevantman, L.H. and Lorenz, J., 1981. *Physical properties data for rock salt* (Vol. 167). US Department of Commerce, National Bureau of Standards.

Kent, P. E. "Recent studies of south Persian salt plugs." AAPG Bulletin 42.12 (1958): 2951-2972.

Lees, G.M., 1927. Salzgletscher in Persien. Mitt. geol. Ges. Wien, 22, pp.29-34.

Peel, F.J., 2014. The engines of gravity-driven movement on passive margins: Quantifying the relative contribution of spreading vs. gravity sliding mechanisms. Tectonophysics, 633, pp.126-142. Doi: 10.1016/j.tecto.2014.06.023

Jackson, M. P. A., & Hudec, M. R. (2005). Stratigraphic record of translation down ramps in a passive-margin salt detachment. Journal of Structural Geology, 27(5), 889–911. Doi: 10.1016/j.jsg.2005.01.010

Jackson, M. P. A., & Hudec, M. R. (2017). Salt tectonics: Principles and practice. Cambridge: Cambridge University Press. Doi: 10.1017/97811 39003988

Jackson, M. P. A., Hudec, M. R., & Dooley, T. P. (2010). Some emerging concepts in salt tectonics in the deepwater Gulf of Mexico: intrusive plumes, canopy-margin thrusts, minibasin triggers and allochthonous fragments. In Vining, B.A., Pickering, S.C., (eds.) Geological Society, London, Petroleum Geology Conference Series, Petroleum Geology: From Mature Basins to New Frontiers – Proceedings of the 7th Petroleum Geology Conference, 7(1), 899–912.

Johnson, T.E., Brown, M., Kaus, B.J.P. & VanTongeren, J.A. 2013. Delamination and recycling of Archaean crust caused by gravitational instabilities. Nature Geoscience, 7, 47, Doi: 10.1038/ngeo2019

Kaus, B.J.P. 2010. Factors that control the angle of shear bands in geodynamic numerical models of brittle deformation. Tectonophysics, 484, 36–47. Doi: 10.1016/j.tecto.2009.08.042

Krueger, S., (2010). Dynamics of tear faults in the salt-detached systems of the Gulf of Mexico [abs.], in. Proceedings AAPG Annual Convention & Exhibition Abstracts, 19, 137–138.

Mukherjee, S., Talbot, C.J. and Koyi, H.A., 2010. Viscosity estimates of salt in the Hormuz and Namakdan salt diapirs, Persian Gulf. *Geological Magazine*, *147* (4), pp.497-507. Doi: 10.1017/S001675680999077X

Peel, F. J., Travis, C. J., & Hossack, J. R. (1995). Genetic Structural Provinces and Salt Tectonics of the Cenozoic Offshore U.S. Gulf of Mexico: A Preliminary Analysis. In M. P. A. Jackson, D. G. Roberts, & S. Snelson (Eds.), Salt Tectonics: A Global Perspective, Vol. 65. Tulsa, OK: American Association of Petroleum Geologists. 153- 175. https://doi.org/10.1306/M65604C7

Pilcher, R. S., Murphy, R. T., & McDonough Ciosek, J. (2014). Jurassic raft tectonics in the northeastern Gulf of Mexico. Interpretation, 2(4), SM39–SM55. https://doi.org/10.1190/INT-2014-0058.1

Ramberg, H., 1981, Gravity, deformation, and the earth's crust: in theory, experiments, and geological application (2d ed). Academic Press, London; New York. 452p.

Rowan, Mark G., Frank J. Peel, and Bruno C. Vendeville. 2004, Gravity-driven fold belts on passive margins, 157-182. In McKley (ed.), Thrust tectonics and Hydrocarbon Systems, AAPG Memoir, Vol. 82. doi: 10.1306/M82813

Rowan, M.G., Peel, F.J., Vendeville, B.C. and Gaullier, V., 2012. Salt tectonics at passive margins: Geology versus models–Discussion. Marine and Petroleum Geology, 37(1), pp.184-194. Doi: 10.1016/j.marpetgeo.2012.04.007

Schultz-Ela, D.D., 2001, Excursus on gravity gliding and gravity spreading, Journal of Structural Geology, Volume 23, Issue 5, 725-731, doi: 10.1016/S0191-8141(01)00004-9.

Schuster, D.C., 1995. Deformation of allochthonous salt and evolution of related salt-structural systems, eastern Louisiana Gulf Coast. In. M. P. A. Jackson, D. G. Roberts, & S. Snelson (Eds.), Salt Tectonics: A Global Perspective, AAPG Memoir, Vol. 65, (pp. 109–151). Tulsa, OK: American Association of Petroleum Geologists.

Talbot, C.J. and Rogers, E.A., 1980. Seasonal movements in a salt glacier in Iran. Science, 208(4442), pp.395-397. Doi: 10.1126/science.208.4442.395

Talbot, C.J. and Jarvis, R.J., 1984. Age, budget and dynamics of an active salt extrusion in Iran. Journal of Structural Geology, 6(5), pp.521-533. Doi: 10.1016/0191-8141(84)90062-2

Talbot, C.J., Medvedev, S., Alavi, M., Shahrivar, H. and Heidari, E., 2000. Salt extrusion at Kuh-e-Jahani, Iran, from June 1994 to November 1997. Geological Society, London, Special Publications, 174(1), pp.93-110. Doi: 10.1144/GSL.SP.1999.174.01.06

Tauvers, P.R., 1993. Salt geometry and kinematics, Texas/Louisiana lower slope, northwest Gulf of Mexico Basin. In Salt, sediment and hydrocarbons. Gulf Coast Section Soc. Econ. Paleontol. Min. Foundation 16th Ann. Conf., pp. 271-274. Doi: 10.5724/gcs.95.16.0271.

Thielmann, M. & Kaus, B.J.P. 2012. Shear heating induced lithospheric-scale localization: Does it result in subduction? Earth and Planetary Science Letters, 359–360, 1–13, Doi: 10.1016/j.epsl.2012.10.002

Turcotte, D.L. and Schubert, G., 2002. Geodynamics. Cambridge University Press. New York. 456 p.

Urai, J.L., Spiers, C.J., Zwart, H.J. and Lister, G.S., 1986. Weakening of rock salt by water during long-term creep. Nature, 324(6097), pp.554-557. Doi: 10.1038/324554a0

Urai, J.L., Schléder, Z., Spiers, C.J. and Kukla, P.A., 2008. Flow and transport properties of salt rocks. *Dynamics of complex intracontinental basins: The central European basin system*, pp.277-290.

Wagner III, B.H. and Jackson, M.P., 2011. Viscous flow during salt welding. *Tectonophysics*, *510*(3-4), pp.309-326. Doi: 10.1016/j.tecto.2011.07.012

Wenkert, D.D., 1979, The flow of salt glaciers. Geophys. Res. Lett., 6: 523-526. doi: 10.1029/GL006i006p00523

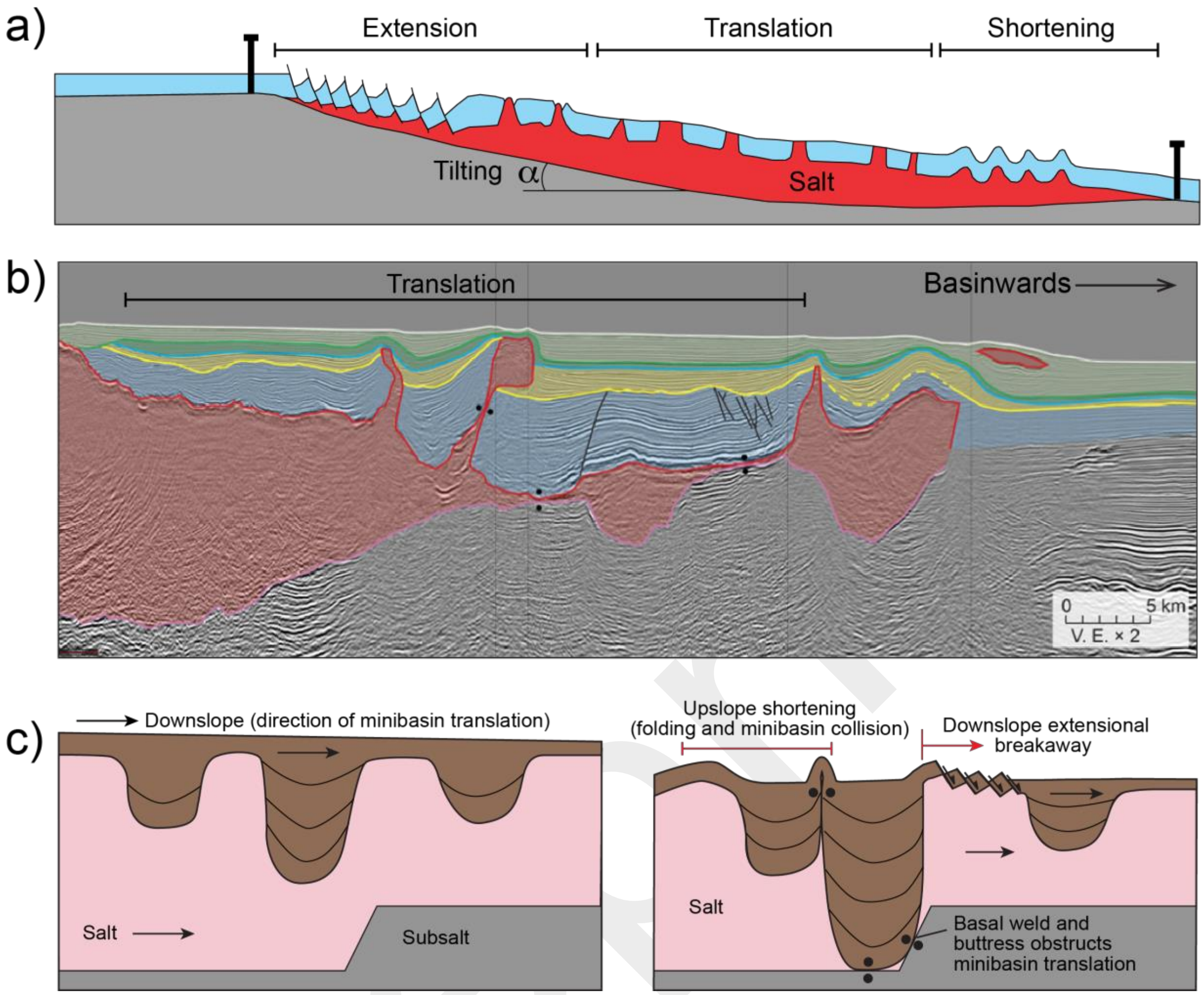

Figure 1. a) Schematic model of a salt-detached slope system with extension-translation-shortening structural zonation. The translational domain is populated with minibasins that translate on top of the salt, as the salt moves downslope. b) Seismic cross section of the Northern Gulf of Mexico, where minibasins of different thicknesses can be observed. These minibasins are at present day, close to the lower portion of the slope and the thickest one is welded at the base. However, these minibasin of different thicknesses may have been nucleated and originated at a position further up the slope from their present-day position. Seismic section is shown with permission from WesternGeco. c) Sketch that illustrates the concept of minibasin obstruction, where, as minibasins translate downslope and get impeded from their translation due to basal weld or buttresses, they get obstructed (Duffy et al., 2020). As salt continues moving around an obstructed minibasin, updip shortening and downdip extension strain patterns develop (modified from Duffy et al., 2020).

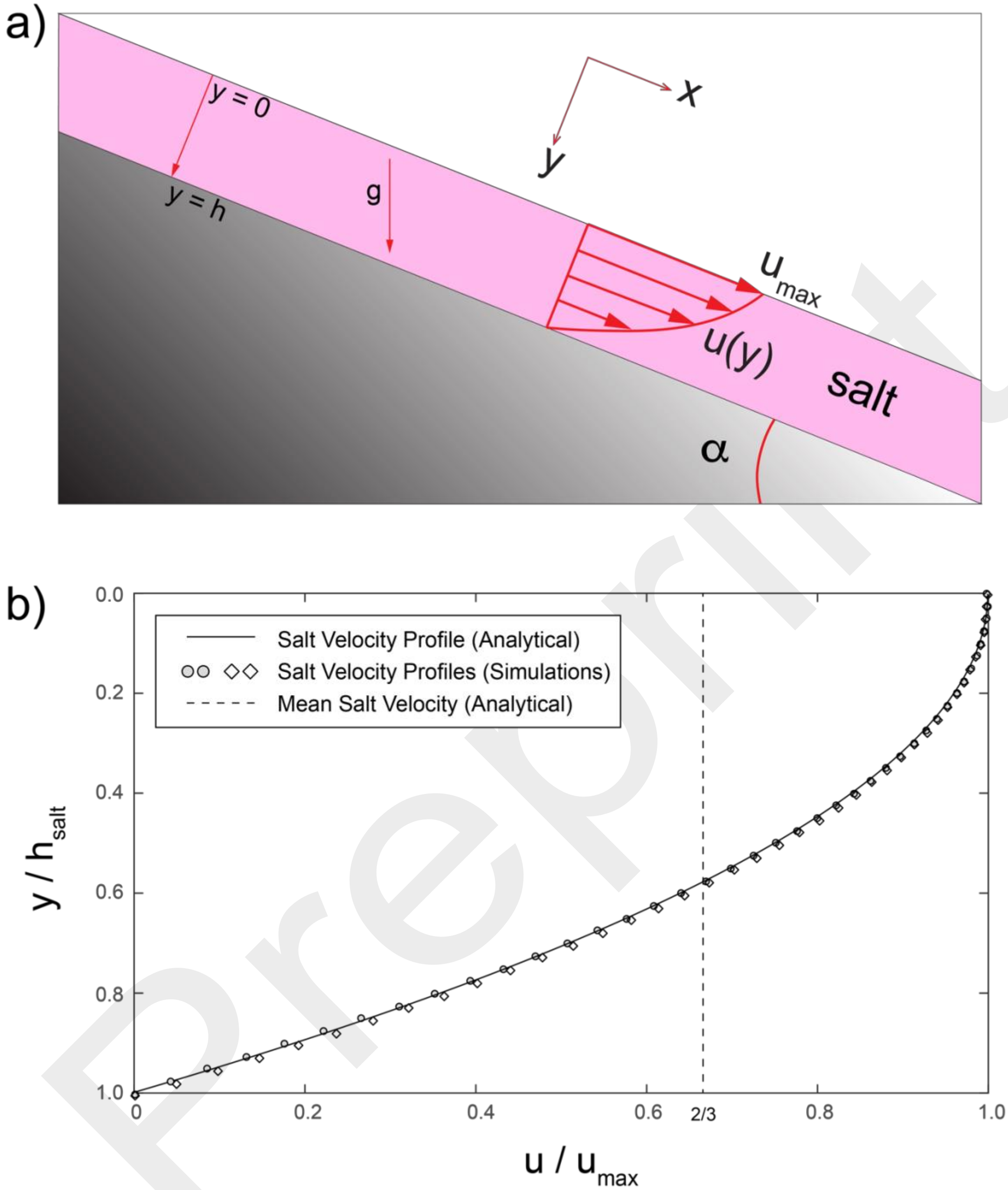

Figure 2. a) Schematic cartoon of a linear viscous salt layer on an inclined plane. The analytical solution assumes that the thickness of the salt layer remains constant. The base of the salt layer has no-slip boundary condition and the top is a free-stress surface. An analytical expression for the resulting velocity profile can be obtained for the given assumptions. b) Comparison between the normalized velocity profile calculated from the analytical expression (continuous line) and the velocities extracted from two different numerical simulations (circles and diamonds). The differences between the numerical and analytical solutions are within %1.

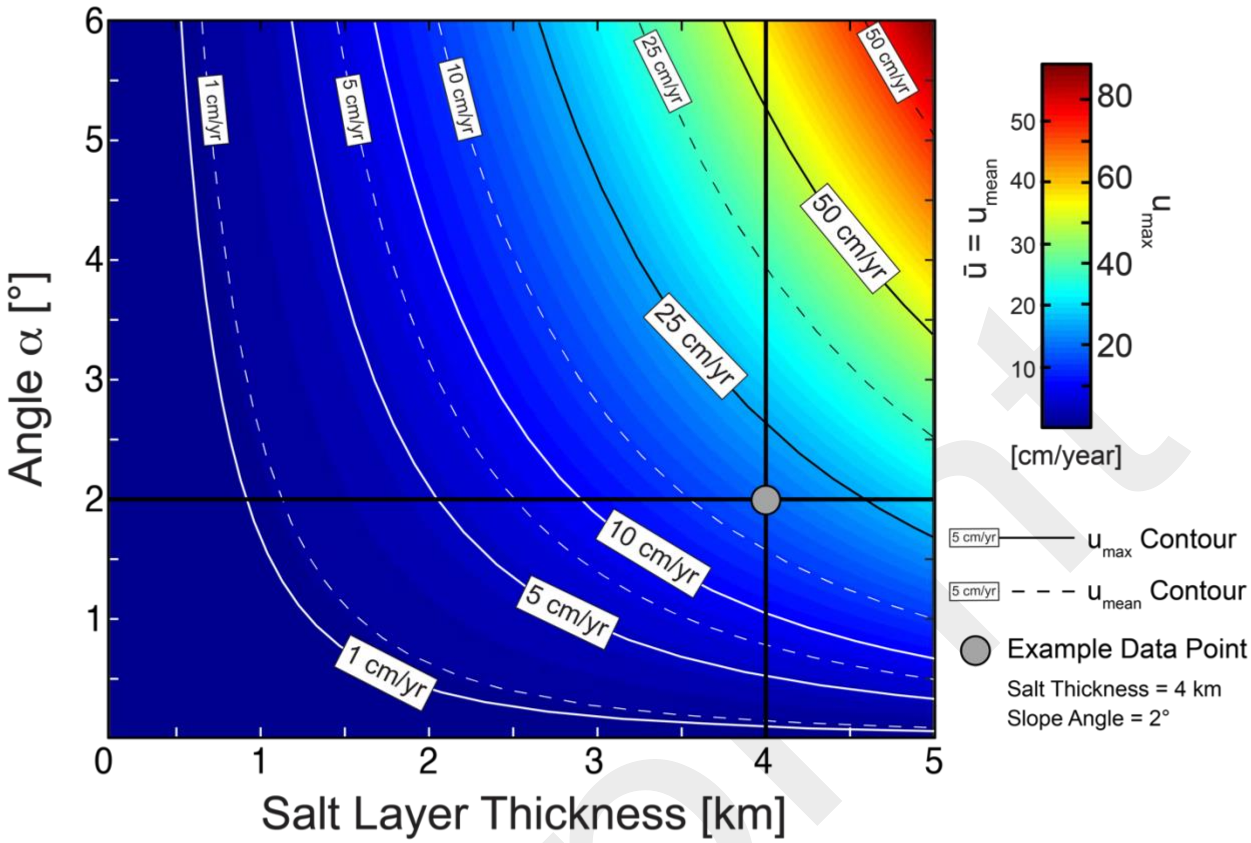

Figure 3. a) Plot of the maximum velocity and mean velocity of the salt layer moving down an inclined plane for a combination of inclination angles and thicknesses of the salt layer. The maximum velocity is obtained at the top of the salt layer. The circle represents the combination of parameters discussed in the text and used in most of the simulations.

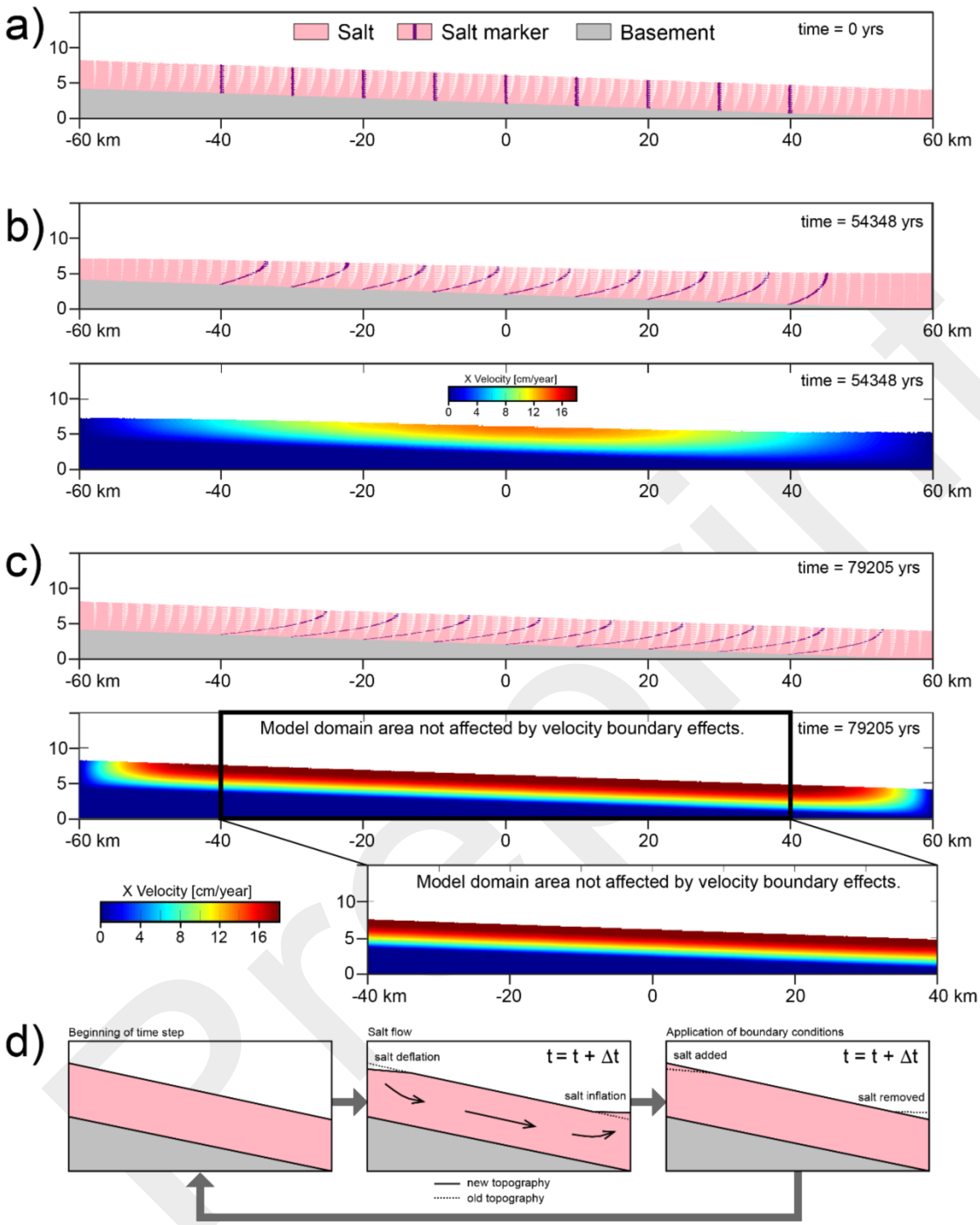

Figure 4. a) Example of an initial model geometry. The modeling box is 120 km x 15 km in size. It contains an inclined basement with a constant thickness layer of salt on top. In this example, the slope angle is α = 2° degrees and salt thickness is H = 4km. b) Intermediate result (geometry in the upper panel and X velocity in the lower panel) of a numerical simulation where the salt is allowed to flow and develop a topography Starting geometry of the numerical simulation is shown in (a). Note the salt deflation at the updip portion of the slope and the salt inflation at the downdip portion of the slope and the extend of the maximum X velocity area localized in the central portion of the slope. c) Intermediate result of a numerical simulation where the salt thickness is kept constant, by applying an internal boundary condition. Note the more homogeneous X velocity profile across the slope compared to (b). The portion of the slope between -40 km and 40 km, is considered to be homogenous and not influenced by edge effects. d) Schematic cartoon (not to scale) illustrating the implementation of the internal boundary condition to keep the salt layer thickness constant. The sketched stages are repeated every time step in the numerical simulations.

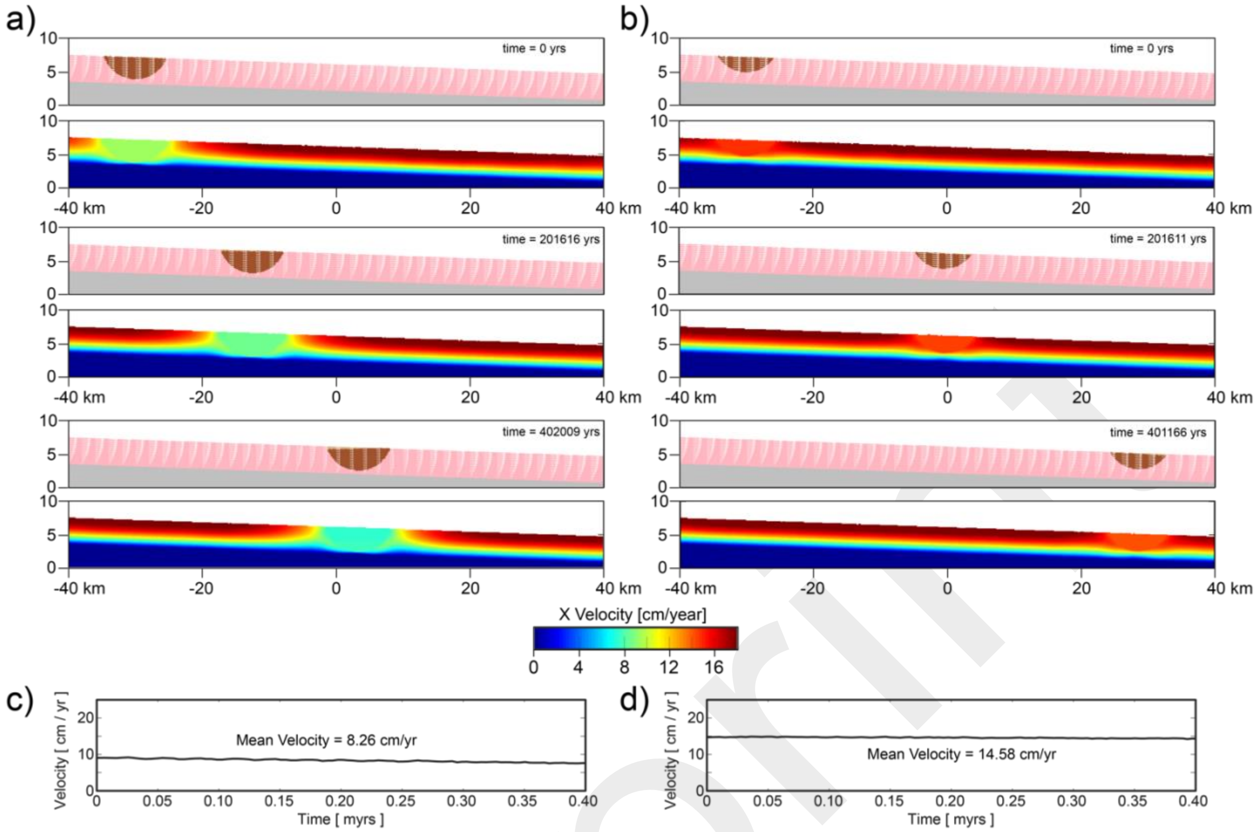

Figure 5. a) and b) Screenshots with plots of composition and velocity field of three different time steps of two numerical simulations of salt moving downslope. a) Simulation with thick minibasin b) Simulation with thin minibasin. c) and d) Graphs with the evolution through time of the mean velocity of the minibasin from the two simulations. c) Simulation with thick minibasin. d) Simulation with thin minibasin. Note that the thin minibasin has higher velocity through time (c) and thus, higher mean velocity than the thick minibasin (d). The higher velocity of the thin minibasin results in the thin minibasin having advanced further than the thick minibasin in the screenshots shown in (a) and (b).

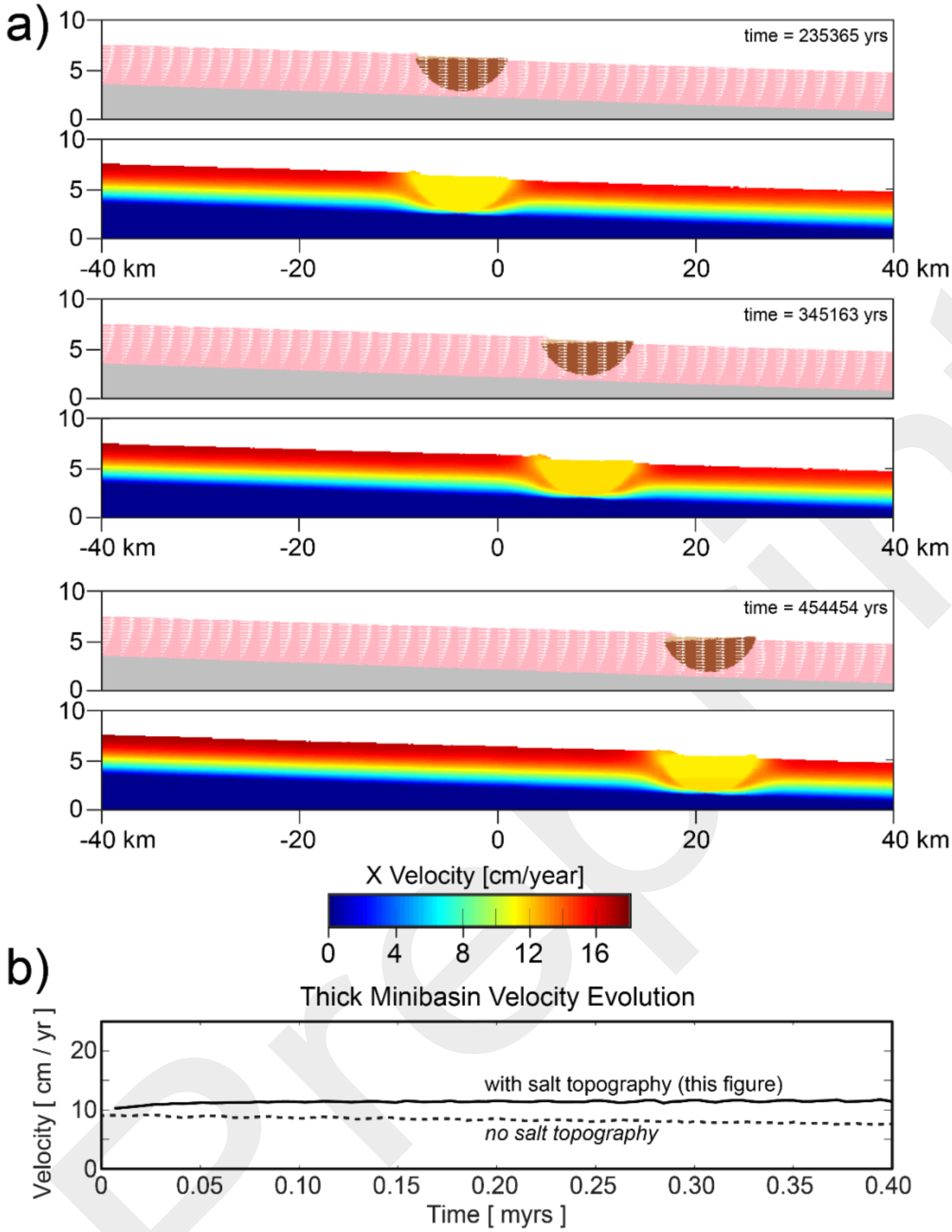

Figure 6. a) Screenshots of four time-step evolution of a numerical simulation with a thick minibasin. In this simulation, implemented boundary conditions, allowed for the development of salt topography. As a result, shallow, faster moving salt is extruded on top of the slow moving minibasin during the translation. b) Graph showing the velocity evolution of the minibasin in the simulation with salt topography (continuous black line, simulation shown in this Figure), and of the minibasin in the simulation with no-salt topography allowed (dashed black line, simulation shown in previous Figure). Note that in the simulation where salt-topography could develop the minibasin velocity increased with time.

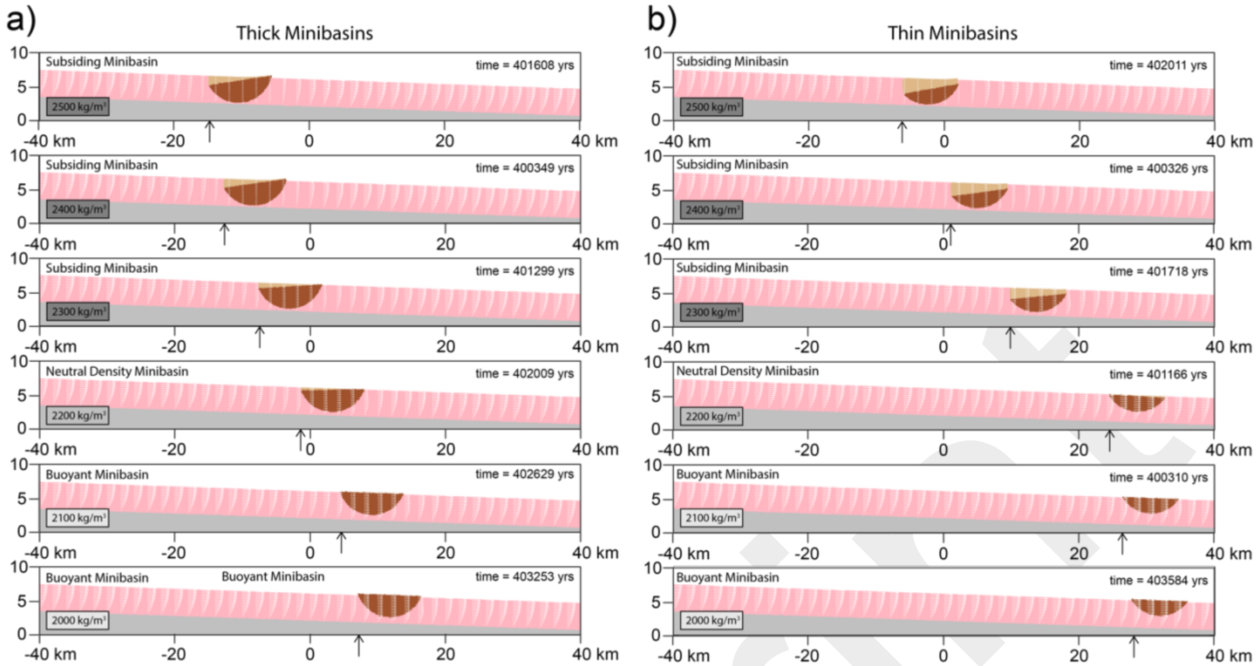

Figure 7. a) and b) Screenshots at the same final time step (time =~400000 yrs.) of numerical simulations with thick (a) and thin (b) minibasins of different densities. The amount of minibasin translation varies according to their densities. Upper panels show the highest density minibasins (denser than salt) and have the least amount of translation (a, b). For simulations with different minibasin densities, final minibasin translation is higher (a, b). Highest minibasin translation is seen at the lower panel (lowest density minibasin, less dense than salt). Minibasins that are denser than salt subside as they translate downslope, allowing for sediment accumulation in their up-slope edge. The accumulation of new sediment results in an increase of minibasin thickness trough time.

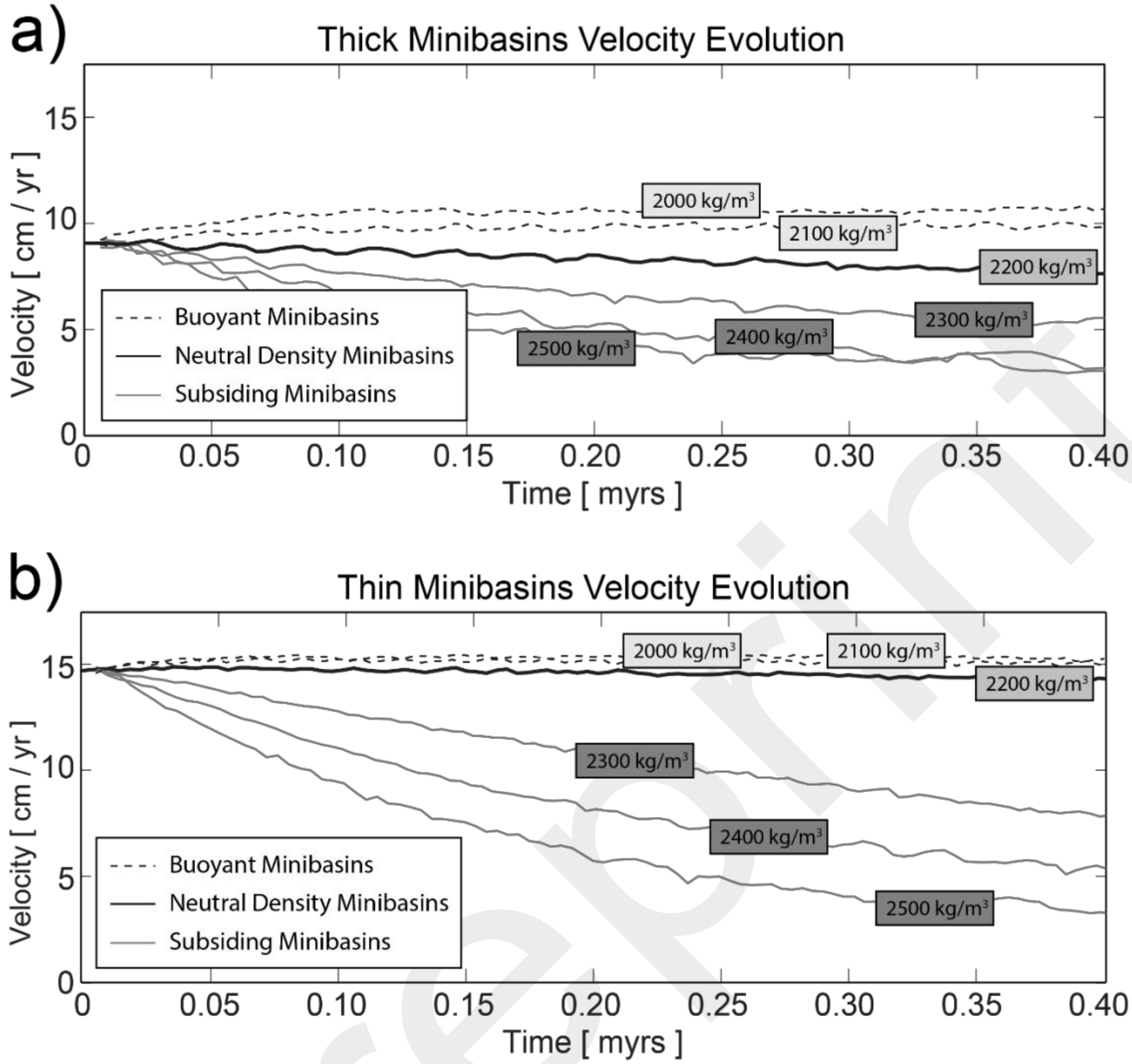

Figure 8. Graphs showing the velocity evolution in simulations with minibasins whose density is different than that of the salt. a) Simulations with thick minibasins. b) Simulations with thin minibasins. Note that, when minibasins are denser than the salt, the velocity of the minibasins tend to decrease through time. Also, the higher the density the faster the decrease in the velocity it is. The opposite is true for minibasins that are less dense than salt, which increase their velocity through time.

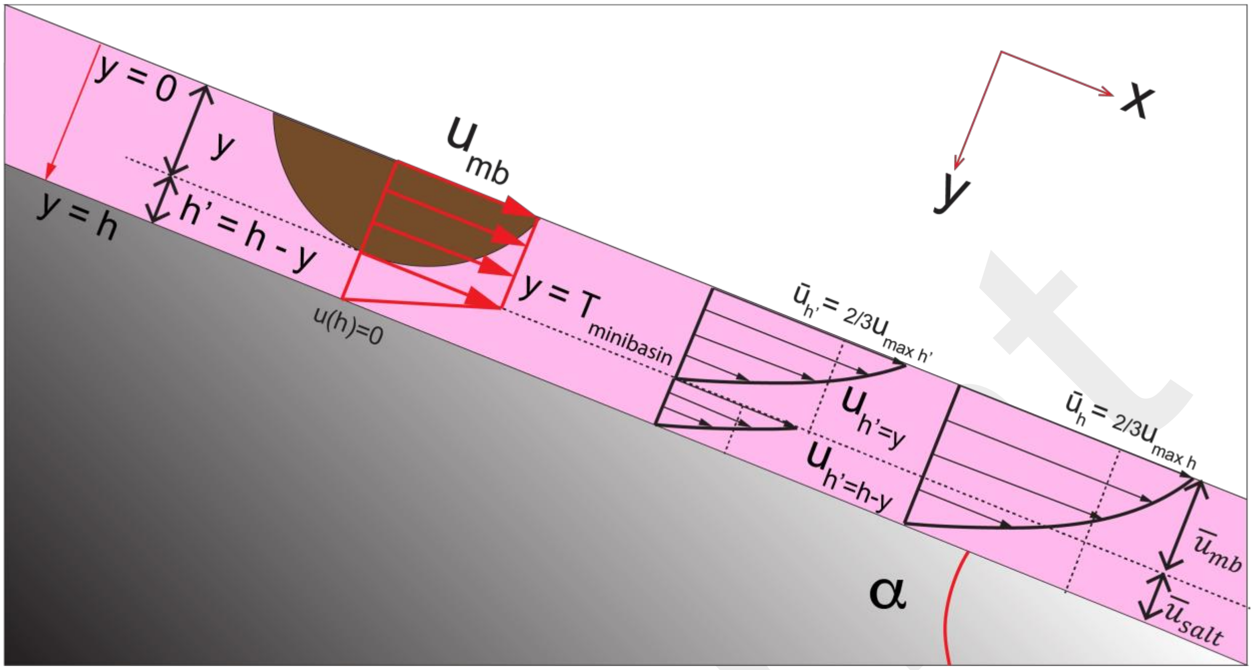

Figure 9. Sketch of a layer of salt on a slope, with a minibasin on it. The position at y, that corresponds to the minibasin thickness $y=T_{mb}$ is used to split the salt layer into two portions: upper salt, $h'=y=T_{mb}$ and lower salt, $h'=h-y$. The velocity profile that would correspond to each portion is shown, together with the theoretical salt velocity profile corresponding to the complete salt layer thickness h. The maximum and mean velocities described in the text are illustrated here. $\overline{u}_{mb}$ corresponds to the mean velocity calculated from the upper portion of the velocity profile, that overlaps with the minibasin thickness. $\overline{u}_{salt}$ corresponds to the mean velocity calculated from the lower portion of the velocity profile that is below the minibasin. Both mean velocities can be obtained by integrating the velocity profile for the corresponding portions.

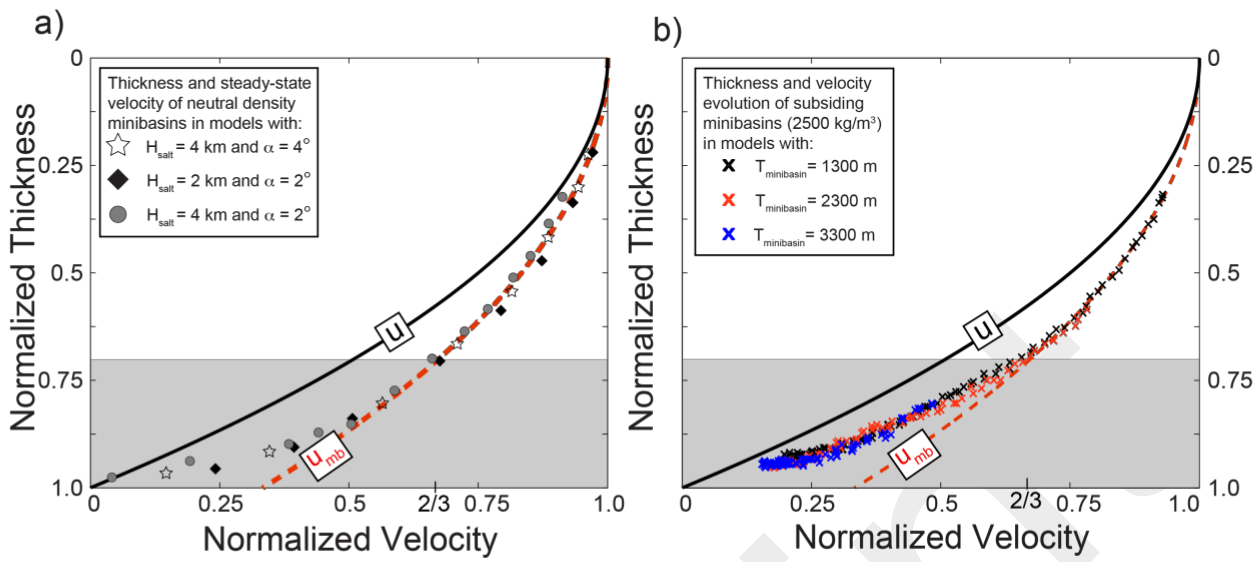

Figure 10. a) Normalized velocity profiles (x axis = $u/u_{max\,h}$; y axis = y/h) calculated with the analytical solution and equations Eq. 1 (black line), 4 (red line) and 5 (blue line), and the various averaged profiles described in the text (dashed lines). Each of the markers (circles, starts, diamonds) correspond to one numerical simulation with neutral-density minibasins of different initial thickness. Three set of parameters were used in the numerical simulations of neutral-density minibasins (each set represented by one type of marker, star, circle or diamond). As noted in the text, neutral-density minibasins, maintain their translation velocity through time, so for each simulation, the minibasin velocity of single (initial) time step is plotted in the normalized graph. Overall, the minibasin velocity of the numerical models fall in a curve that relates the salt velocity at the base of the minibasin, and the mean velocity of the portion corresponding to the minibasin thickness (red dashed line). Only, when the initial minibasin thickness is close to the thickness of the salt layer (T_{mb} > 0.7h; greyed area), the velocity is lower than predicted in by the curve, and the results plot in a different trend in the graph. b) Normalized velocity profiles (same as in a). Markers (crosses) indicate the minibasin velocity and thickness evolution through time of three simulations in which the minibasin is denser than salt, and thus subsiding. The velocity of subsiding minibasins decreases through time, as they subside and become thicker (see text for details). Overall the velocity and thickness evolution of subsiding minibasins follow a trajectory as described by the analytical curve (red dashed line), until they reach a certain thickness (shaded gray). When the minibasin thickness is closer to the salt thickness (and close to the base-of-salt), the minibasin translation velocity decreases more dramatically.

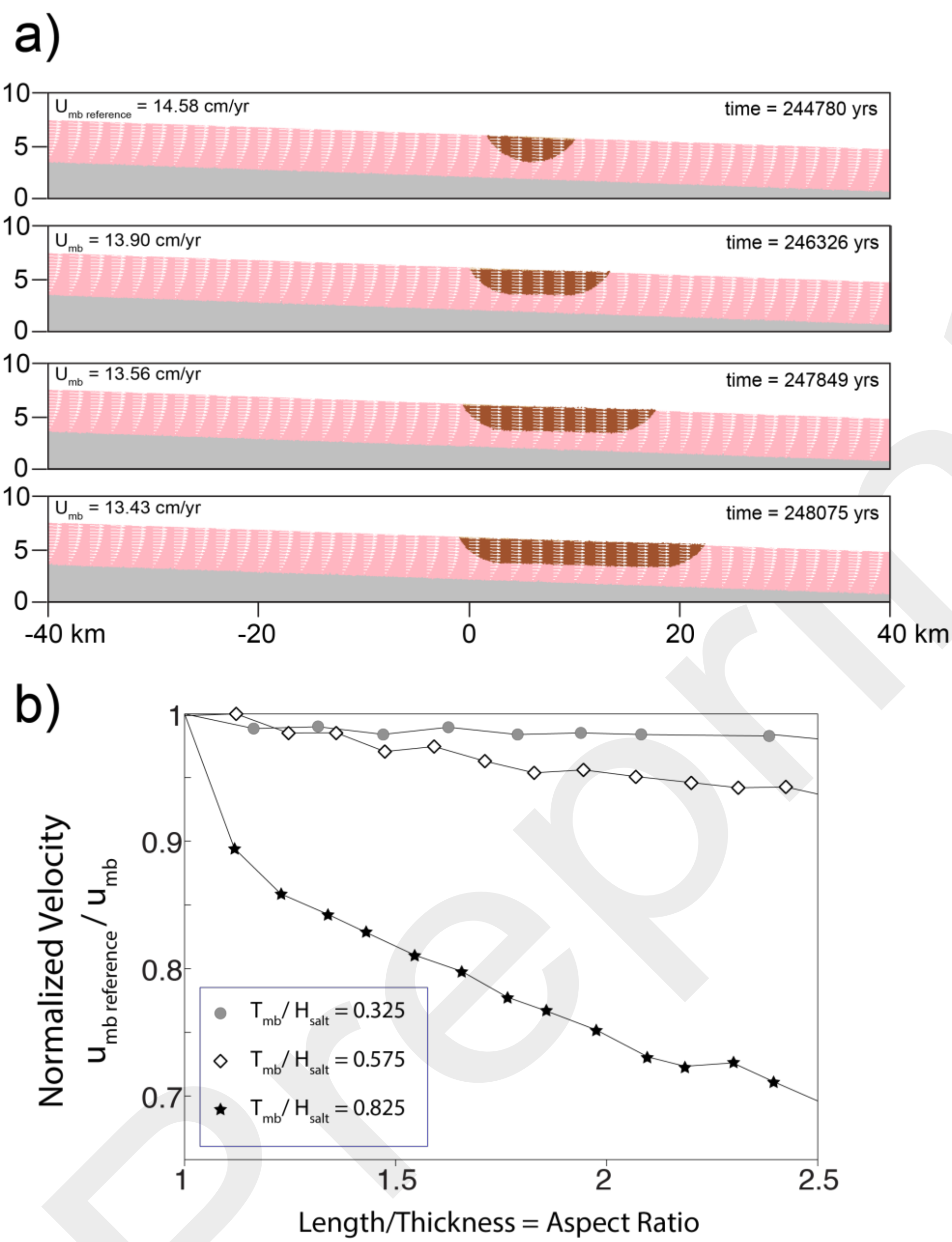

Figure 11. a) Screenshots at the same time-step of four simulations with neutral-density minibasins of same initial thickness but different length or aspect ratio. The minibasin to salt thickness of this example is T_{mb}/H_{salt} = 0.575. The arrow indicates the center of the minibasin, which at the beginning of the simulations was located at the same position for all for cases. The arrow at this time step illustrates, that although there has been differential translation, the amount is relatively small. The longest minibasin, which has the highest aspect ratio, (lower panel) has the slowest mean velocity of all, although the differences are relatively small. b) Graph showing the relation between the aspect ratio and minibasin velocity, for neutral buoyancy minibasins with three different initial thicknesses. Each point is one simulation. Each marker type (start, diamond, circle) corresponds to one thickness (e.g. diamond shaped markers correspond to thicknesses shown in (a)). The velocity is normalized to illustrate a decrease from the reference velocity (given by the minibasin with the smallest aspect ratio. Overall, the higher the aspect ratio is, the lower the translation velocity is. However, as discussed in text, thickest minibasins, show a higher effect of the aspect ratio.

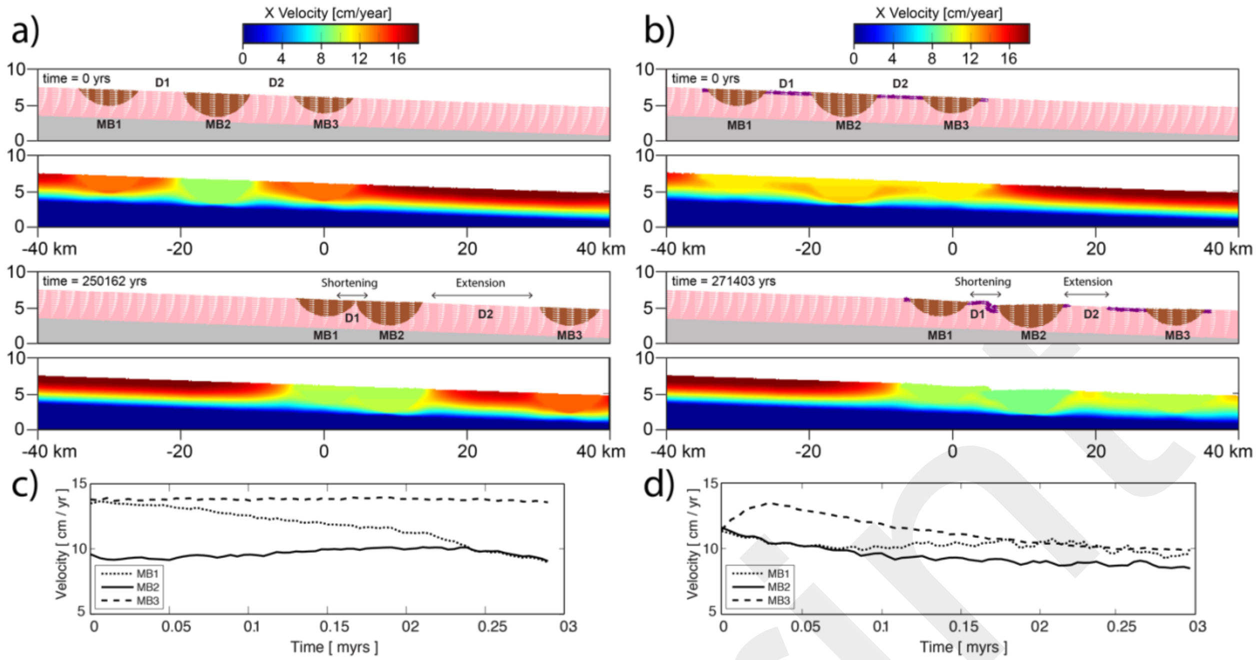

Figure 12. Screenshots of a three time-step evolution of a chain of three neutral-density minibasins on a slope (from updip to downdip, MB1, MB2 and M3; with intervening diapirs D1 and D2). The minibasin in the center (MB2) is thicker than the ones updip and downdip. Two scenarios are shown. One scenario in which the diapirs are exposed and not covered by a roof (a), and one in which the diapirs are covered by a roof on top (b). The velocities of the minibasins for each scenario are plotted in c) and d). In the simulation with the exposed diapirs (a), as the numerical simulation evolves, the thin minibasins (MB1 and MB3) translate faster than the thick minibasin (MB2) (c). However as the simulation evolves, updip thin minibasin (MB1), decreses its velocity as it approaches the thick minibasin MB2 (c). In the simulation with covered diapirs (b), because the three minibasins are initially connected by the roof, their starting velocities are the same (d). However, as the simulation evolves, the downdip minibasin (MB3) drifts away from the minibasin in the center (MB2), the roof in between the two gets stretched (b,d). Instead, the minibasin updip (MB1), converges towards the minibasin in the center and the roof in between gets shortened by folding (b,c).

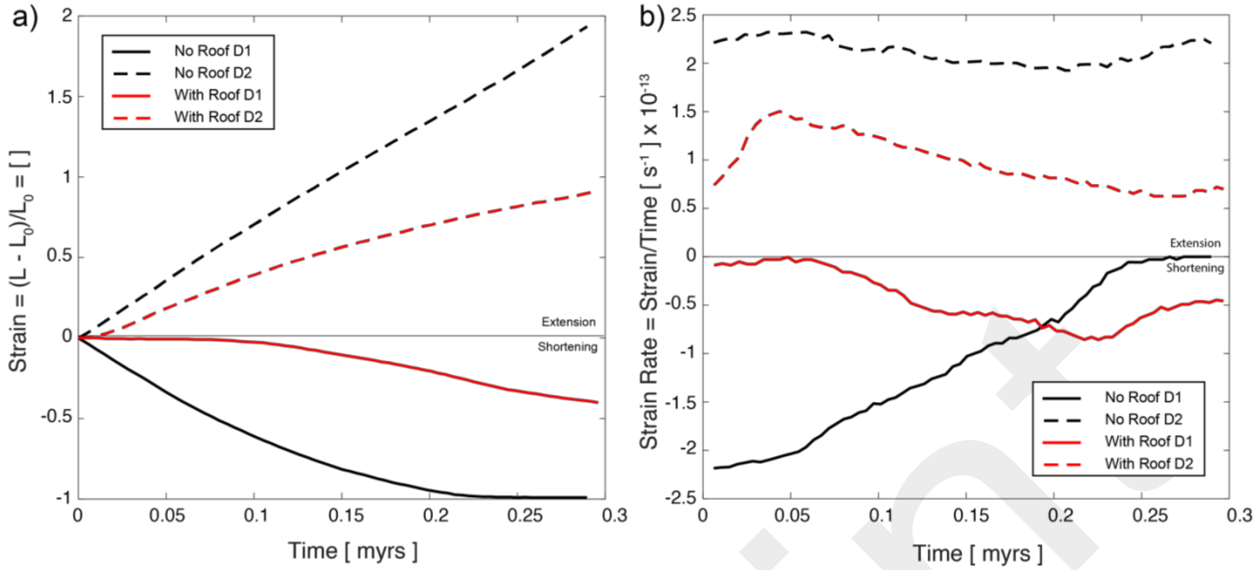

Figure 13. a) Strain accommodated by the diapirs D1 and D2, for the simulations with no roof and without roof. D1 is the diapir located upslope, in between the converging minibasins MB1 and MB2. As such, diapir D1 accommodates the shortening, as shown by negative value of the strain. The opposite is true for diapir D2, which is located downslope, between diverging minibasins MB2 and MB3. It must also be noted, the higher amount of strain, whether extensional or compressional, accommodated by the case in which the diapir has no roof. b) Strain rate calculated for the diapirs D1 and D2. The negative value of the strain rate indicates the shortening which is being accommodated by diapir D1. Notice, how in the case of the diapir with roof, the strain rate remains close to zero initially, meaning that there is no strain being accommodated by the roof. This is very different to what it is observed in the case with roof. Additionally, in the case of the diapir D2, both the cases with roof and no-roof start accommodating the deformation early in their evolution.

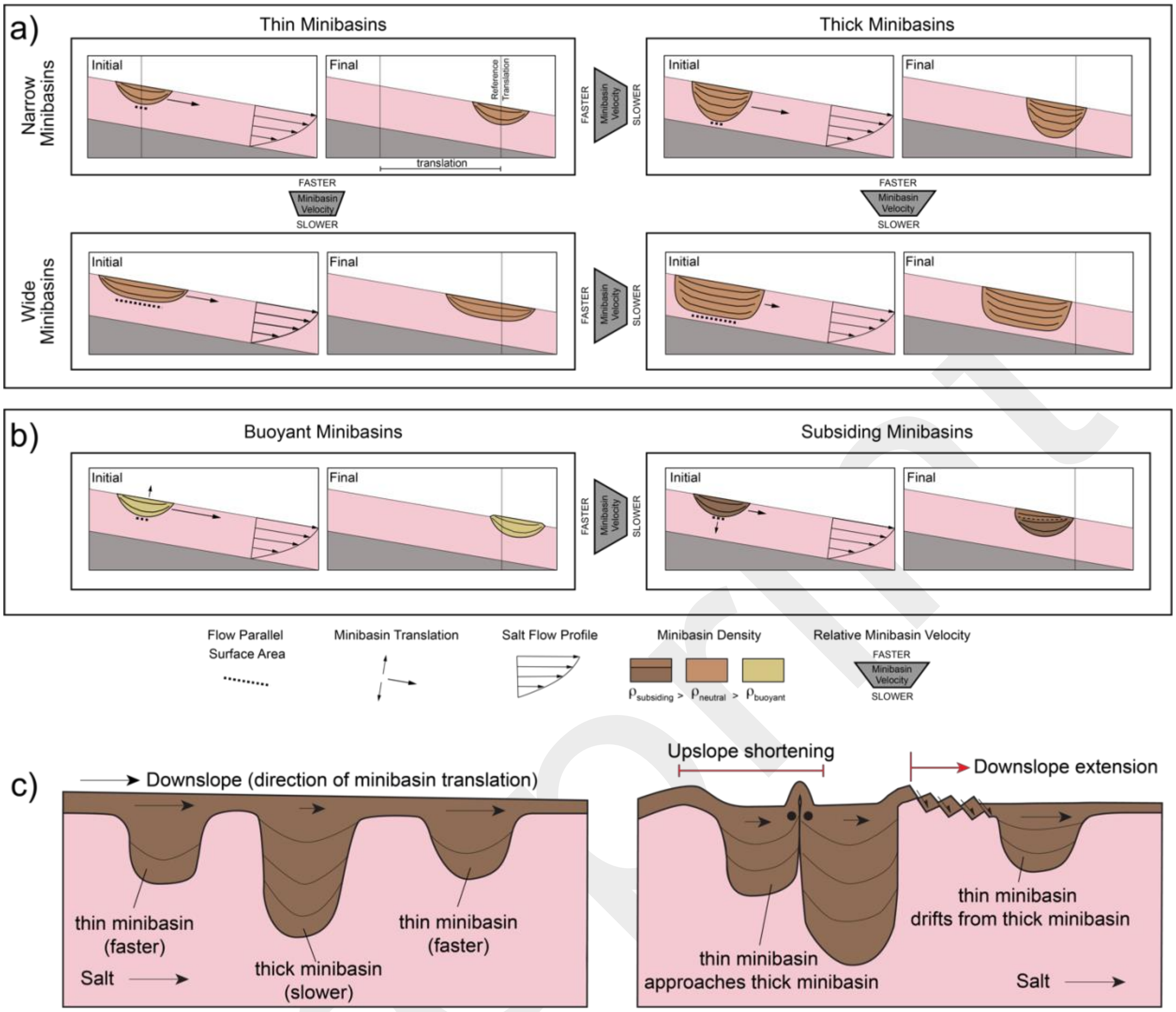

Figure 14. Conceptual sketches reviewing the main controls on minibasin velocity in the numerical simulations with neutral-density minibasins (a) and buoyant and subsiding minibasins (b). a) The main control on minibasin velocity in the case of neutral-density minibasins is the minibasin thickness (or distance to base-of-salt). Thicker minibasins have a lower translation velocity and thus will cover less translation distance for the given time, when compared to thinner minibasins. For a minibasin of a given thickness, its width (measured as an aspect ratio, width to thickness) also influences the translation velocity. A wider minibasin, translates slower than a narrow one. The velocity decrease due to higher flow parallel surface area, is even more dramatic in the case of thick minibasins. b) Minibasins that are either buoyant or subsiding will change the distance from the base-of-salt as they translate. Subsiding minibasins create accommodation space for new sediments and increase their thickness, thus reducing their distance from the base of the salt, and ultimately reducing their translation velocity. c) Sketch illustrating that minibasins translating at different velocities can result at similar strain patterns of updip shortening and downdip extension without minibasin obstruction.

Appendix A: Derivation of Equations

A1. 1D channel flow

Here, we reproduce the steps as described in Turcotte and Schubert (2002) to derive the general expression for the velocity profile, *u(y)* of a viscous fluid in a channel that has the configuration shown in Fig. A1. Where τ indicates shear stress, and p, indicates pressure.

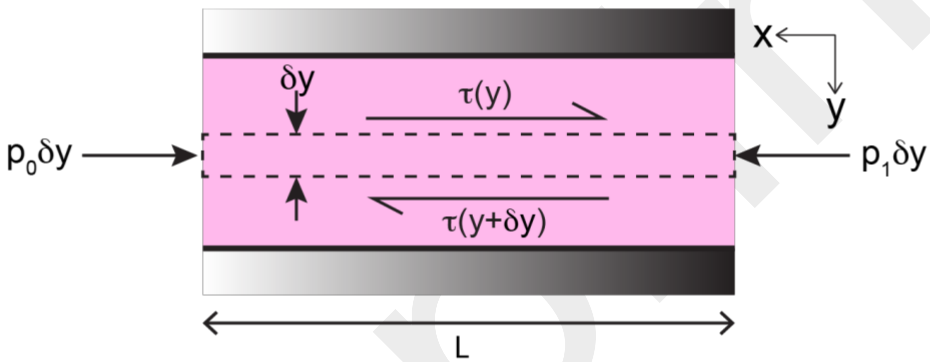

Figure A1. Force balance in a channel with a viscous fluid (in pink) and pressure gradient in the x direction.

In the case of linear viscous fluids (with constant viscosity, μ), the shear stress, τ , at any location of the channel is given by:

$$\frac{du}{dy}\mu = \tau \qquad \text{(A1)}$$

The viscosity of the fluid, μ, is the constant of proportionality between the shear stress, τ, and the strain rate or velocity gradient, $\frac{du}{dy}$.

Flow in channel can be determined by the equation of motion, which implies a force balance on a layer of fluid of thickness δy and length L.

Net pressure force on the element in x direction is $(p_1 - p_0)\,\delta y$, which is the force per unit depth in the direction normal to the plane. For a 1-D channel flow, shear stress and velocity depend only on y.

Shear force on upper boundary of layer is $-\tau(y)L$ and at he lower boundary in x direction is:

$$\tau(y + \delta y)L = \left(\tau(y) + \frac{d\tau}{dy}\,\delta y\right) L \qquad \text{(A2)}$$

The net force in the layer is zero so we can rewrite as follows:

$$(p_1 - p_0)\delta y + \left(\tau(y) + \frac{d\tau}{dy}\,\delta y\right) L - \tau(y)L = 0 \qquad \text{(A3)}$$

$$\frac{d\tau}{dy} = -\frac{(p_1 - p_0)}{L} \qquad \text{(A4)}$$

$$\frac{dp}{dx} = -\frac{(p_1 - p_0)}{L} \qquad \text{(A5)}$$

$$\frac{d\tau}{dy} = \frac{dp}{dx} \qquad \text{(A6)}$$

By substituting $\frac{du}{dy}\mu = \tau$ in Eq. (A6), we obtain:

$$\mu\frac{d^2\tau}{dy^2} = \frac{dp}{dx} \qquad \text{(A7)}$$

Integration of the equation gives,

$$u = \frac{1}{\mu}\frac{dp}{dx}y^2 + C_1 y + C_2 \qquad \text{(A8)}$$

To evaluate the constants, we use the following boundary conditions, of u(h) = 0 and u(0) = u_0, which gives us the following general expression for the velocity in a 1D channel:

$$u = \frac{1}{2\mu}\frac{dp}{dx}(y^2 - hy) - \frac{u_0 y}{h} + u_0 \qquad \text{(A9)}$$

By substituting the Eq. (A9) into the Eq. (A1) of shear stress for viscous flows a general expression for the shear stress in a 1D channel is obtained:

$$\tau = \frac{1}{2}\frac{dp}{dx}(2y - h) - \frac{u_0 \mu}{h} \qquad \text{(A10)}$$

A2. 1D channel flow on an inclined plane

Now, instead of a horizontal channel, let's consider a constant thickness (h) layer of viscous fluid resting on an inclined plane as given in the Fig. A2.

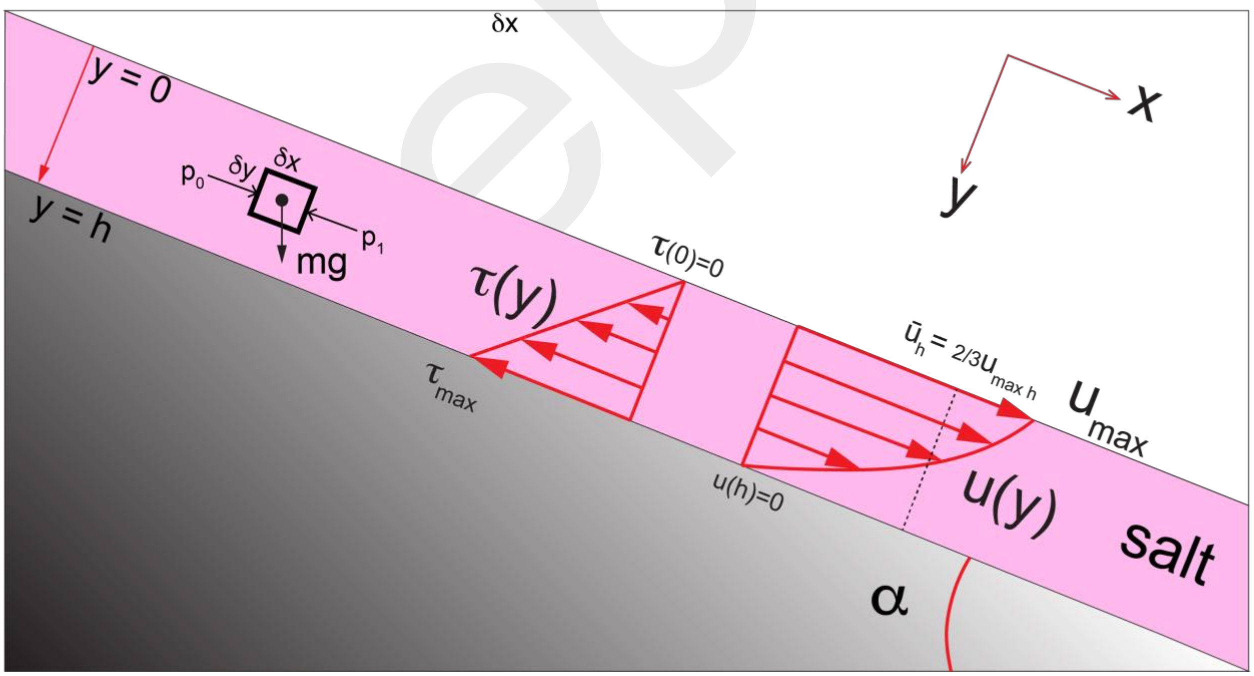

Figure A2. Viscous fluid of constant thickness (in pink) resting on an inclined plane. The force balance in the channel is shown in a small element of dimensions δx, δy. Assuming a free-surface at the top and no-slip at the base of the viscous layer, the resulting velocity and shear stresses are shown.

We will again follow the steps given by Turcotte and Schubert (2002). First, we calculate the pressure gradient in the channel. If we consider a small unit element inside the channel with dimension of δx , δy and in equilibrium, the force in x is given by,

$$F_x = m\ g\ sin\alpha = \delta x\ \delta y\ \rho\ g\ sin\alpha \qquad \text{(A11)}$$

We can then calculate the pressure gradient along the x direction (parallel to the slope) as:

$$p_1 = p_0 + \frac{F_x}{\delta y} \qquad \text{(A12)}$$

$$\delta p = p_0 - p_1 = p_0 - \left(p_0 + \frac{\delta x\ \delta y\ \rho\ g\ sin\alpha}{\delta y}\right) = -\delta x\ \ \rho\ g\ sin\alpha \qquad \text{(A13)}$$

We can rearrange the equation as:

$$\frac{\delta p}{\delta x} = -\rho\ g\ sin\alpha \qquad \text{(A14)}$$

which is the pressure gradient in x direction due to the slope.

We can substitute the pressure gradient in the previously defined equation of motion in a channel due to pressure gradient (section A1) to obtain:

$$\frac{d\tau}{dy} = -\rho\ g\ sin\alpha \qquad \text{(A15)}$$

By integrating Eq. (A15), we can obtain $\tau(y)$ as:

$$\tau(y) = \int_0^y -\rho\ g\ sin\alpha\ \ dy = -\rho\ g\ sin\alpha\ y + C_1 \qquad \text{(A16)}$$

Assuming free-surface at y = 0, then $\tau(0) = 0$, then C_1 = 0.

Which gives a linear shear stress profile, increasing from 0 at the free surface to maximum shear stress at the no-slip base.

As given in Eq. (A1), for linear viscous fluids, we can relate the velocity gradient to the shear stress by the proportionality constant given by the viscosity, which is shown rewritten here:

$$\frac{du}{dy} = \frac{\tau}{\mu} \qquad \text{(A17)}$$

We can use Eq. (A16) and Eq. (17) to obtain the following:

$$u(y) = \int_0^y \frac{\tau}{\mu}\, dy = -\int_0^y \frac{\rho\, g\, sin\alpha\, y}{\mu}\, dy = \frac{\rho\, g\, sin\alpha\, y^2}{\mu\, 2} + C_2 \qquad \text{(A18)}$$

Assuming no-slip boundary condition at base u(h) = 0, then $C_2 = \frac{\rho\, g\, sin\alpha\, h^2}{\mu\, 2}$. The velocity profile of a constant thickness viscous layer on an inclined plane is given by:

$$u(y) = \frac{\rho\, g\, sin\alpha\, y^2}{\mu\, 2} + \frac{\rho\, g\, sin\alpha\, h^2}{\mu\, 2} = \frac{\rho\, g\, sin\alpha}{\mu\, 2}\,(h^2 + y^2) \qquad \text{(A19) or } \textbf{Eq. (1)}$$

The velocity profile that results from a constant thickness layer with a free surface at the top, is not linear, but parabolic (as seen in the picture).

The maximum velocity at this case, occurs at the free-surface (y=0) where the shear stress is zero.

$$u_{\max\, h} = u(0) = \frac{\rho\, g\, sin\alpha\, h^2}{\mu\, 2} \qquad \text{(A20) or } \textbf{Eq. (2)}$$

And the mean velocity can be obtained by integrating the velocity profile for the layer thickness and dividing it by the thickness.

$$u_{mean\,h} = \bar{u}_h = \frac{1}{h}\int_0^y u(y)\ dy = \frac{\rho\, g\, sin\alpha\, h^2}{\mu\, 3} = \frac{2}{3}u_{\max\,h}$$ (A21) or **Eq. (3)**

Equations (1), (2) and (3) are the ones used in the main text.

A3. Velocity profiles for (sub-)layers defined within an inclined viscous layer

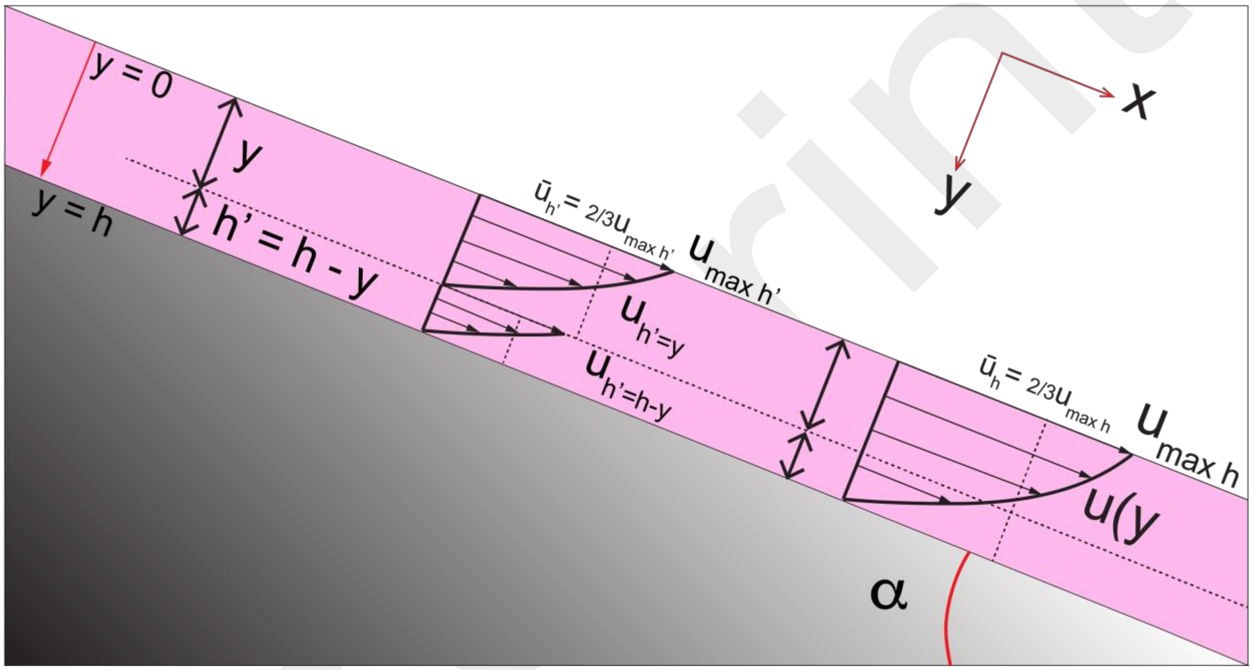

Figure A3. Schematic illustration of the resulting velocity profiles when instead of the total thickness (h) of the viscous layer, partial thicknesses are considered. Upper portion where h'=y and lower portion where h'=h-y.

Now, instead of considering one unique velocity profile for the layer thickness of h of the entire viscous layer, we will consider the velocity profiles for (sub-)layers whose thicknesses, h', range between 0 and y (h'=y) and between y and h (h'=h-y) (see Fig. A3). In the case of h' = y, the maximum and mean velocities of the viscous (sub-)layers with thicknesses between 0 and y, can be calculated as:

$$u_{\max\,h'=y} = \frac{\rho\, g\, sin\alpha\, (y)^2}{\mu\, 2}$$ (A22)

$$u_{\mathrm{mean}\ h'} = \bar{u}_{\,h'=y} \ = \frac{\rho\ g\ sin\alpha\ (y)^2}{\mu\ 3} \qquad \text{(A23)}$$

Subtracting $u_{\max at\ y}$ from $u_{\max for\ h}$ gives the $u(y)$ of Eq. (A19) or Eq. (1):

$$u_{\max\ h} - u_{\max\ h'=y} = u(y) \qquad \text{(A24)}$$

Additionally, we consider the case of layers whose thicknesses h’, range between y and h (h’=h-y). In this case, instead of having a unique value for the maximum and mean velocities, we have a range of values as given by:

$$u_{\max\ h'=h-y} = \frac{\rho\ g\ sin\alpha\ (h\prime)^2}{\mu\ 2} = \ \frac{\rho\ g\ sin\alpha\ (h-y)^2}{\mu\ 2} \qquad \text{(A25)}$$

$$\bar{u}_{\,h'=h-y} \ = \ \frac{\rho\ g\ sin\alpha\ \left(h'\right)^2}{\mu\ 3} = \frac{\rho\ g\ sin\alpha\ (h-y)^2}{\mu\ 3} \qquad \text{(A26)}$$

A4. Minibasin on an inclined viscous layer

All the calculations in the previous sections consider the 1D flow channel equations. However, in the numerical models presented in the main text, minibasins are present in the slope. We will consider the minibasin being of the same density as the fluid, but a much higher viscosity (10^{25} Pa s). The viscosity of the minibasins is so high compared to the surrounding viscous fluid, that it effectively behaves as a rigid body, and it will translate down slope with a homogeneous velocity. These minibasins have a finite lateral extend, so there is a variation of velocity and shear stress along the x direction, which is not considered in the 1D channel flow equations. Despite this along X variation in velocity and shear stress, we can try to relate the minibasin velocity obtained from the models with the equations of 1D channel flows.

As in the previous section, we consider the viscous layer as divided in two portions from 0 to y and from y to h, but now we consider that y corresponds to the minibasin thickness, T_{mb}. See Fig. A4. The salt layer is then divided between 0 and $y=T_{mb}$ and between $y=T_{mb}$ and h. We will refer to these portions of the minibasin layer as upper portion and lower salt layer portion.

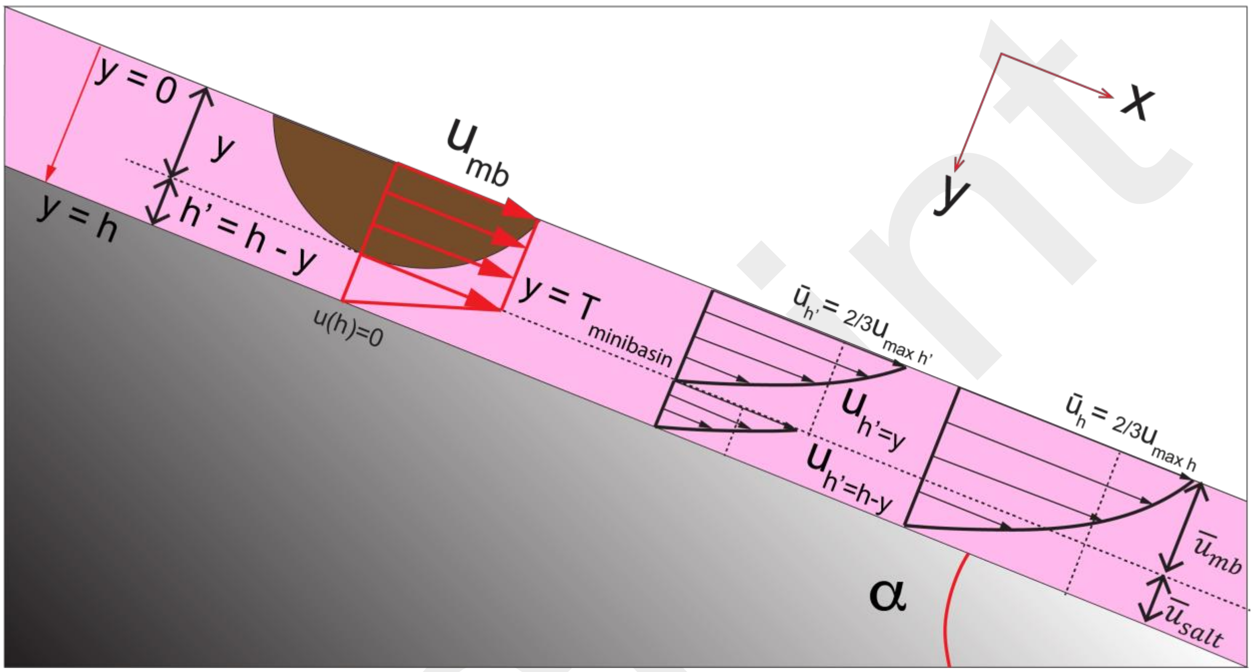

Figure A4. Schematic illustration of the viscous layer (in pink) resting on an inclined plane. A minibasin (in brown) of density equal to that of the viscous fluid with a circular geometry is present in the viscous fluid. The thickness of the minibasin is $T_{mb.}$

The minibasins of the numerical simulations shown in this work, are sub-circular in shape, as illustrated in Fig. A4. However, we can also consider, rectangular shape minibasins with vertical walls and flat base as shown in Fig. A5.

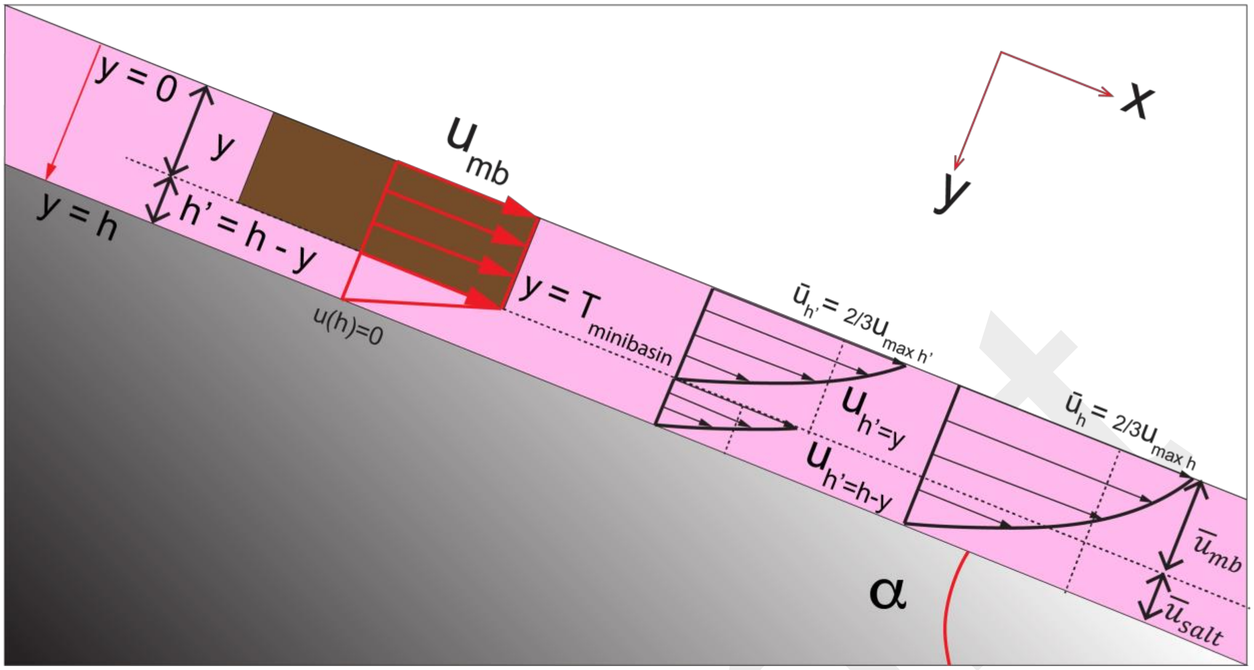

Figure A5. Schematic illustration of the viscous layer (in pink) resting on an inclined plane. A minibasin (in brown) of density equal to that of the viscous fluid with a rectangular geometry is present in the viscous fluid. The thickness of the minibasin is T_{mb}.

Let's first consider the salt velocity profile calculated for the full thickness of the salt (h) and calculate the mean velocity of salt layer corresponding to the portions covering the minibasin thickness (upper portion) and the thickness below the minibasin (lower portion). We will call these velocities $\bar{u}_{mb}$ and $\bar{u}_{salt}$ respectively.

$$\bar{u}_{mb} = \frac{1}{y}\int_0^y u\,\partial y = \frac{1}{y}\,\frac{\rho\, g\, sin\alpha}{2\mu}\left(h^2 y - \frac{y^3}{3}\right) \qquad \text{(A27)}$$

$$\bar{u}_{salt} = \frac{1}{h-y}\int_{h-y}^{h} u\,\partial y = \frac{1}{h-y}\,\frac{\rho\, g\, sin\alpha}{2\mu}\left(\frac{2h^3}{3} - h^2 y - \frac{y^3}{3}\right) \qquad \text{(A28)}$$

Similarly, we can consider the equations from the previous section, where we calculated the maximum and mean velocity for viscous layers of thickness between 0 and h'=y, but now we consider y = T_{mb}.

$$u_{\max\ y=Tmb} = \frac{\rho\ g\ sin\alpha\ (y)^2}{\mu\ 2} \qquad \text{(A29)}$$

$$\bar{u}_{y=Tmb} = \frac{\rho\ g\ sin\alpha\ (y)^2}{\mu\ 3} \qquad \text{(A30)}$$

The equations for 1D channel flows are plotted in a normalized graph. The x-axis represents the velocities, normalized over the maximum velocity for a free-surface. T y-axis represents the thickness of a sub-portion of the total layer of thickness, normalized over the total thickness of the layer (h).

The results from the numerical simulations with minibasins can be plotted on the graph with the theoretical equations (minibasin velocity and thickness). Similarly, results of numerical models of rafts or sediment blocks (vertical walls, instead of circular walls) are plotted.

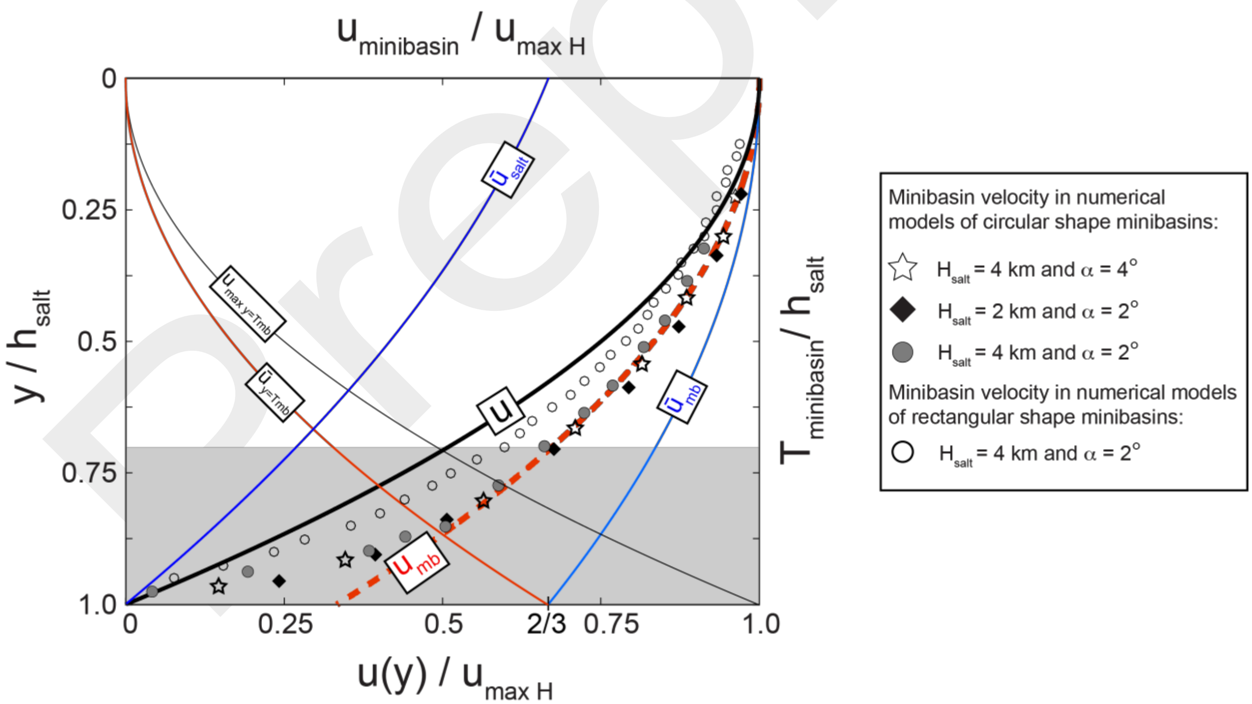

Figure A4. Normalized plot with the solid-line graphs corresponding to the 1D channel flow derived equations as described in the text. Markers correspond to results of 2D numerical simulations with rectangular minibasins (hollow circles) and circular minibasins (grey circles, black diamonds, hollow starts) for the simulation parameters shown in the legend.

The numerical models show that thin minibasins translate faster than thick minibasins. The relation between thickness and minibasin velocity in the case of minibasins of circular shape describes a curve in the graph. In fact, the results from the numerical simulations with minibasins plot on top of a curve that can be described by the following equation,

$$u_{mb} = u_{\max h} - \bar{u}_{y=Tmb} = \frac{\rho\ g\ sin\alpha\ h^2}{\mu\ 2} - \frac{\rho\ g\ sin\alpha\ y^2}{\mu\ 3} \qquad \text{(A31) or } \textbf{Eq. (4)}$$

Eq. (4) is used in the main text to predict the velocity of sub-circular minibasins in the numerical simulations.

However, the minibasins with a rectangular shape (vertical walls), plot closer to the graph described by $u(y)$. In addition, Increasing the length (width) of the minibasin, but keeping their thickness the same, reduces minibasin velocity, moving the velocity value in the graph to the left. The lower limit for the velocity of a minibasin of given thickness is the velocity described by u(y). The velocities calculated in numerical simulations with minibasins of different geometries (aspect ratios, sub-circular or rectangular), plot in the area of the graph between $u(y)$ and u_{mb}.

Thus, although the equations are derived for 1D channel flows, they can be used to predict the velocity of sub-circular minibasins as shown in the main text.

References

Turcotte, D.L. and Schubert, G., 2002. Geodynamics. Cambridge University Press. New York. 456 p.